Canadian Geotechnical Journal

Research Article

Particle morphology and principal stress direction dependent strength anisotropy through torsional shear testing

Shao-Heng He[a], **Zhen-Yu Yin**[a,b], **Zhi Ding**[c], **and Rui-Dong Li**[a]

[a]Department of Civil and Environmental Engineering, The Hong Kong Polytechnic University, Hung Hom, Kowloon, Hong Kong 999077, China; [b]Research Centre for Resources Engineering towards Carbon Neutrality (RCRE), The Hong Kong Polytechnic University, Hung Hom, Kowloon, Hong Kong 999077, China; [c]Department of Civil Engineering, Hangzhou City University, Hangzhou 310015, China

Corresponding author: **Zhen-Yu Yin** (email: zhenyu.yin@polyu.edu.hk)

Abstract

The major principal stress direction angle (α_σ) experienced by granular soils varies widely in engineering, causing different strengths. However, how particle morphology affects the strength anisotropy behavior under different α_σ remains unclear. To address this gap, this study performed drained hollow cylinder torsional shear tests under different α_σ on six granular materials with distinct morphologies. Results highlight the significant dependence of peak strengths of granular materials on both particle morphology and α_σ. Increasing particle shape irregularity and surface roughness leads to a considerable enhancement in peak strength, while this peak strength significantly degrades with increasing α_σ. Materials with more irregular shapes were found to have a more pronounced strength anisotropy. Furthermore, the initial fabric of particle packings, derived from three-dimensional X-ray microtomography, was used to interpret microscopic mechanisms behind the morphology-dependent strength anisotropy. Irregular-shaped materials display broader preferred particle orientations and higher initial fabric anisotropy compared to relatively regular-shaped materials. This higher morphology-induced fabric anisotropy contributes to strength anisotropy, and a correlation was established for describing this trend. Additionally, an anisotropic failure criterion incorporating fabric anisotropy was developed to characterize the strength envelope for granular materials with diverse shapes.

Key words: granular materials, hollow cylinder torsional shear, X-ray microtomography, shear strength

1. Introduction

The strength behavior of granular material is significantly influenced by the orientation of principal stress axes, leading to variability and anisotropy in their strength characteristics (Mandolini et al. 2019). For instance, when the major principal stress is perpendicular to the orientation of the major axis of grains, the peak strength of sands is typically higher compared to when the major principal stress is parallel to the direction of grain alignment (Yang et al. 2015*a*). Strength anisotropy, often referred to as the variation in peak strength with respect to the direction of the principal stress, is a phenomenon commonly observed for sandy soils and holds great importance in engineering applications (Lade et al. 2014).

Understanding and accounting for the anisotropic behavior of graunlar materials is vital for accurate geotechnical mechanical modeling and design of structures on sandy soils, such as retaining walls, slopes, embankments, and offshore structures (He et al. 2023). For instance, in a slope stability analysis where the inclination of the major principal stress of soils across different slope regions varies from 0° to 90° (see Fig. 5*a*), the strength variation and anisotropy can affect the critical failure surface and the corresponding factor of safety. Several studies have been performed to comprehend this subject, with hollow cylinder apparatus (HCA) proving to be a useful tool to investigate the anisotropic strength of sandy soils (Zhuang et al. 2022). This apparatus is particularly valuable due to its capability to conduct shear tests across a range of principal stress orientations. By fixing the principal stresses at an inclined angle in HCA shear tests, researchers can simulate the stress conditions that occur in field and measure the resulting shear strength of soils. Miura et al. (1986*a*), Xiong et al. (2016), and Cai et al. (2018*b*) observed considerable strength anisotropy of sands using HCA shear tests on Toyoura sand under different major principal stress direction angles (α_σ). Their findings suggested that as α_σ increases, the peak strength of sand initially drops, reaching the lowest value at α_σ=60°–75°, and then slightly increases or stabilizes. Likewise, Lade et al. (2014) reported similar results for Nevada sand. However, Zdravkovic and Jardine (2000) and Kumruzzaman and Yin (2010), respectively, noted that the

peak strength of Ham river sand and Hong Kong completely decomposed granite (CDG) sand continuously reduces with α_σ. The differences may arise due to the variations in the type and properties of sand used, as well as the testing procedures and conditions. Additionally, Shibuya et al. (2003) performed HCA shear tests on Ham River sand to investigate its undrained anisotropy and undrained monotonic response. They reported the presence of significant undrained anisotropy in sand samples, and suggested that the sand's undrained anisotropy and cyclic response can be interpreted by the concept of an undrained local boundary surface. Moreover, Uthayakumar and Vaid (1998) investigated the dependence of the sand's undrained behavior on the orientation of principal stresses relative to the bedding planes (i.e., a plane perpendicular to the direction of particle deposition), using hollow cylinder torsional shear tests under generalized loading paths. They observed that the susceptibility of sand to liquefaction due to stress rotation increases as the major principal stress aligns more closely with the orientation of the bedding plane. Overall, the mechanical anisotropy of sandy soils remains a significant phenomenon that gains ongoing interest of geotechnical researchers and practitioners.

Particle morphology is acknowledged to play a fundamental role in the mechanical properties and internal structure of sandy soils (Huo et al. 2023; Liu et al. 2023, 2024*b*; Banerjee et al. 2024). Numerous studies have investigated the impact of particle shape on soil mechanics (Rui et al. 2020, 2021; He et al. 2024). For instance, according to the triaxial tests conducted by Sarkar et al. (2019), Xiao et al. (2023), and Li et al. (2024), it was found that angular particles tend to provide interlocking between grains, resulting in higher shear strength compared to rounded particles. In direct shear tests, Liu et al. (2024*a*) discovered a robust linear correlation between particle width, shape, and the internal friction angle. Specifically, roundness was found to be negatively associated with the internal friction angle, while particle width showed a positive correlation with it. Based on discrete element method (DEM) simulation results of triaxial tests on samples with different particle shapes, Liu et al. (2024*b*) reported that as the shape of the particles becomes increasingly deviated from spherical, the interlocking is enhanced, and stronger contact force will be generated along the loading direction, causing the increase of shear strength. Additionally, the potential for increased inter-particle friction to enhance strength has been emphasized in the existing literature (Li et al. 2019; Xiao et al. 2019, 2023; Reddy et al. 2022). With an increase in angularity of the particles, the combined effect of fabric and force-induced anisotropy contributes to the greater strength of the sand assemblies (Azéma et al. 2012, 2013). On the other hand, the relationships between various morphological factors and mechanical parameters have been extensively established based on well-controlled experimental and DEM investigations (Li 2013; Yang and Luo 2015; Altuhafi et al. 2016; Nguyen et al. 2020; Adesina et al. 2024; Gong et al. 2024). Besides, Zhao et al. (2017) conducted a numerical investigation of particle shape effects on fabric of granular packing using the three-dimensional (3D) DEM with a super-ellipsoid model. Their simulation results indicate that particle shape has a significant effect on the anisotropy of both particle orientations and contact normals. Through two-dimensional DEM simulations of granular materials with varied particle shapes, Adesina et al. (2024) have reported that contact fabric anisotropy, the magnitude of moments transmitted between particles, and the friction mobilized at contacts are pivotal factors that underpin material strength. The geometry of particles affects how they stack and interact with each other, ultimately determining the overall fabric and behavior of the material. However, the existing understanding of how particle shape affects mechanical behavior has primarily come from experiments, like triaxial tests, or numerical simulations, without explicitly considering the varying orientations of the principal stress axis. There have been few investigations into the influence of particle shape on mechanical behavior under inclined principal stress axes through hollow cylinder torsional shear tests (Yang et al. 2015*b*).

The degradation and direction-dependent anisotropy of strength in sandy soils can be attributed to the different relative angles between the varying fabric/orientation of particle depostion along a preferential direction and different major principal stress directions. Previous studies have demonstrated that the internal orientation/fabric of particle depostion is primarily influenced by the specimen preparation method and particle shape (Oda 1972; Yang et al. 2008). These two key factors can impact the soil's ability to resist shear stress in different directions, leading to varied strengths. Through a 2D image-analysis-based technique, Yang et al. (2008) and Shi et al. (2021) quantified the inherent fabrics of laboratory-prepared sand specimens using different sample preparation methods. They discovered that the long axes of the particles tend to align horizontally as a result of gravitational deposition during the sample preparation process. During the specimen preparation process, particularly when employing methods like moist tamping, the energy applied to the material results in an adjustment of particle orientation, thereby potentially leading to increased heterogeneity (Gu et al. 2021). The preferred particle orientation during specimen preparation process can result in the anisotropic mechanical properties of the material under different principal stress directions. Unfortunately, the existing research primarily focuses on specimen preparation methods while neglecting to evaluate the impact of particle shape on mechanical anisotropy. Furthermore, there is a dearth of studies examining the influence of particle shape on the internal microstructure of particle assembly using objective measurements. This lack of investigation has contributed to the obscure understanding of the mechanism behind particle shape's effect on mechanical anisotropy. The uncertainty surrounding the anisotropic factors of strength in natural granular materials with diverse morphologies creates difficulties in directly applying existing correlations between strength parameters and morphological parameters derived from commonly used tests without inclined major principal axes. Furthermore, this uncertainty raises doubts about the applicability of existing failure criteria for uniformly describing the strength of distinct-shaped granular materials. As a result, it is crucial to conduct further research to gain a comprehensive understanding of the mechanical anisotropy exhibited

by granular materials with varying morphologies to prevent unsafe designs of geotechnical structures.

This study provides a comprehensive range of experimental data and evidence on the mechanical behavior of granular materials under drained monotonic HCTS tests with various inclined major principal stress axes. This study employs six granular materials with measured particle morphology indices for comparative analysis, with a focus on interpreting mechanism and modeling the role of particle morphology in mechanical anisotropy. Moreover, high-resolution 3D images of particle packing are obtained using X-ray microtomography, providing insights into the microscopic mechanism of mechanical anisotropy through internal fabric/particle orientation. Correlations between fabric anisotropy, particle morphological factors, and strength anisotropy are established. Additionally, an anisotropic failure criterion is proposed and verified to characterize the strength envelope for granular materials with diverse shapes. The experimental data on natural sand are crucial for developing constitutive models, while the tests on round glass beads will aid in numerical simulations at the particle-scale based on the discrete element modeling (DEM).

2. Test materials and methods

2.1. Test materials and particle morphology recognitions

Figure 1 displays six types of granular materials with varying morphologies utilized in this study, including four artificially manufactured glass beads (i.e., round, frosted, concave, and convex glass beads) and two natural sands (i.e., Fujian standard sand and Hong Kong CDG sand), all of which are particles with a same particle size distribution (see Fig. 2*a*). The production of frosted glass beads involves using machinery equipped with diamond grit to rotate and polish the glass beads, resulting in a uniformly rough surface on the glass beads. Fujian sand is renowned as the standard sand in China, while CDG sand derived from the in situ weathering granitic rocks is extensively distributed in Hong Kong.

The Nikon XT H225ST 2X Computed Tomography (CT) system was used to determine the particle shape of granular materials (Gapinski et al. 2014). During the scanning process, the particles were horizontally positioned on a rotational manipulator stage (He et al. 2024). The X-rays traversed the sample, producing a silhouette image on the detector, known as a projection. In this study, a comprehensive dataset of 3000 projections was collected over a full 360° rotation to ensure the acquisition of high-resolution imagery. These projections were converted to gray-level CT images by the 3D CT reconstruction software, Inspect-X. The obtained CT images underwent initial processing with median and Gaussian filters to mitigate the effects of noise, following the methodologies outlined by (Ito and Xiong 2000). Afterward, thresholding segmentation was used to transform gray-scale images into binarized images where the value of 0 represented the background, and 1 indicated the presence of particles. The H-extreme watershed algorithm was then used to segment the connected particles into 3D separate ones (Burgmann et al. 2022). Finally, the marching cube algorithm was adopted to transform the particles into triangle meshes that could be used for subsequent 3D particle shape indices analysis (Lorensen and Cline 1998). Additionally, the 2D shape indices of particles from all six materials were assessed and determined using 2D horizontal cross-sections of the CT images, which clearly depicted surface characteristics. The 2D shape indices were derived based on the two different programs or scripts including ImageJ software and the MATLAB script of Zheng and Hryciw (2015). To ensure accuracy, 3D and 2D particle morphological factors were meticulously calculated for hundreds of individual particles from each material. Four commonly used particle shape indices (Altuhafi et al. 2013; He et al. 2022), i.e., sphericity (S), aspect ratio (AR), convexity (C), and roundness (R) were determined for each material. As illustrated Fig. 3, S denotes the ratio of the perimeter of a circle with the same area as the projected area of the grain to its actual perimeter; AR is the ratio between the maximum diameter (D_{max}) and the minimum diameter (D_{min}); C is defined as the area of the grain (S_A) divided by the area if any concavities within its perimeter are filled (i.e., $S_A + S_B$); R is calculated as the ratio of the average of surface feature curvature radii to the radius of the maximum inscribed sphere.

The surface roughness of six granular materials, quantified by the average roughness (R_a) and root mean square roughness (R_q), was measured using a CounourGT-K optical interferometer with the vertical resolution of 0.01 nm and horizontal resolution of 0.38 μm (He et al. 2024). The center of each particle was employed in the roughness measurement to prevent inaccuracies caused by the particle's edges and curvatures. The definitions of R_a and R_q are demonsrated in Fig. 2*b*, where M and N are numbers of pixels in X and Y directions; Z_{ij} is the height of a point to the mean plane of the surface. Table 1 provides a summary of S, C, AR, R, and R_a, as well as various physical indices, such as index void ratios, for each material. Note that the majority of previous studies have utilized 2D particle shape indices to establish the correlation with strength parameters (Sarkar et al. 2019; Xiao et al. 2019, 2023). Accordingly, this study also employs two-dimensional particle shape indices to establish the relationship between particle morphology and the anisotropy of strength and fabric, facilitating comparison with existing research.

2.2. Test methods and programs

As shown in Fig. 4, a commercial HCA with the design similar to that of the apparatus used by Cai et al. (2018*b*) was adopted in this study. The stress and strain state of a soil element including the vertical stress/strain (σ_z/ε_z), radial stress/strain (σ_r/ε_r), circumferential stress/strain ($\sigma_\theta/\varepsilon_\theta$), and torsional shear stress/strain ($\tau_{z\theta}/\gamma_{z\theta}$) is depicted in Fig. 5*b* and calculated using equations in Table 2. Moreover, Table 2 also includes the equations for calculating the generalized deviatoric stress q and deviatoric strain γ_g. The intermediate principal stress coefficient $b = (\sigma_2 - \sigma_3)/(\sigma_1 - \sigma_3)$ represents the effect of the intermediate principal stress (σ_2) on the response of a soil element under major principal stress, σ_1, and minor

Fig. 1. Microscopic images for six granular materials: (*a*) round glass bead; (*b*) frosted glass bead; (*c*) concave glass bead; (*d*) convex glass bead; (*e*) Fujian sand; and (*f*) completely decomposed granite sand.

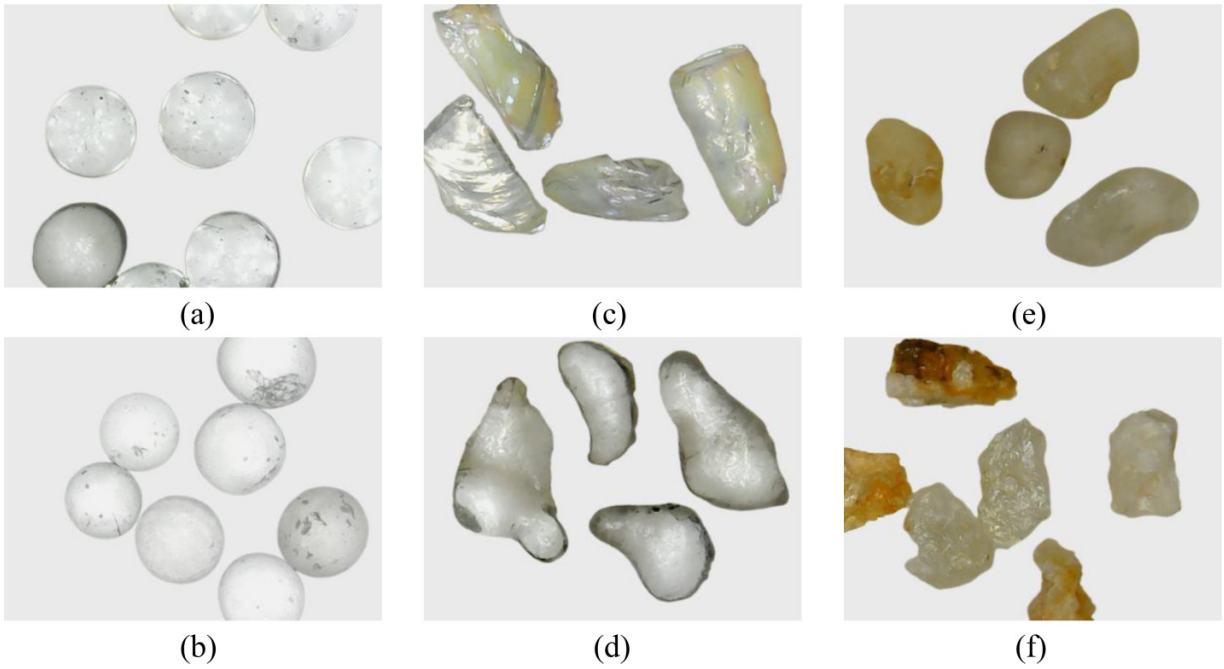

Fig. 2. Particle size distribution and definition of roughness: (*a*) particle size distribution and (*b*) roughness.

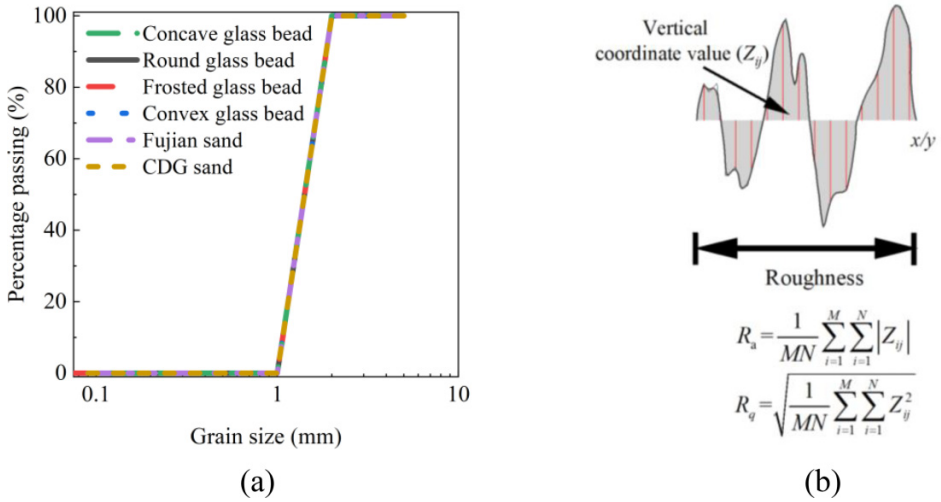

principal stress, σ_3. Figure 5*d* depicts the definitions of angles for major principal stress direction α_σ, major principal strain increment direction $\alpha_{d\varepsilon}$, and the noncoaxiality angle β. They are all calculable using the formulas below:

$$(1)\quad \alpha_\sigma = \frac{1}{2}\arctan\left(\frac{2\tau_{z\theta}}{\sigma_z - \sigma_\theta}\right)$$

$$(2)\quad \alpha_{d\varepsilon} = \frac{1}{2}\arctan\left(\frac{d\gamma_{z\theta}}{d\varepsilon_z - d\varepsilon_\theta}\right)$$

$$(3)\quad \beta = \alpha_{d\varepsilon} - \alpha_\sigma$$

The hollow cylinder specimens have an inner diameter of 60 mm, an outer diameter of 100 mm, and a height of 200 mm. The dry tamping method, which is described in detail in Chen et al. (2021), was employed to prepare specimens. To achieve a high saturation level, the specimen was flown with carbon dioxide and de-aired water and subjected to back pressure saturation until the *B*-value exceeded 0.95. To conduct the *B*-value test, an increment of 20 kPa was applied to the effective confining pressure ($\Delta p'$) under undrained conditions, resulting in a measured pore pressure increment denoted as $\Delta\mu$. The *B*-value is subsequently calculated using the equation $B = \Delta\mu/\Delta p'$. The initial D_r of the specimens composed of various granular materials is uniformly set within the range of $D_r \approx 86\%$–89% for comparative analysis.

Fig. 3. Schematic for definitions of particle shape indices: (*a*) aspect ratio; (*b*) convexity; (*c*) sphericity; and (*d*) roundness (modified from Lashkari et al. (2020)).

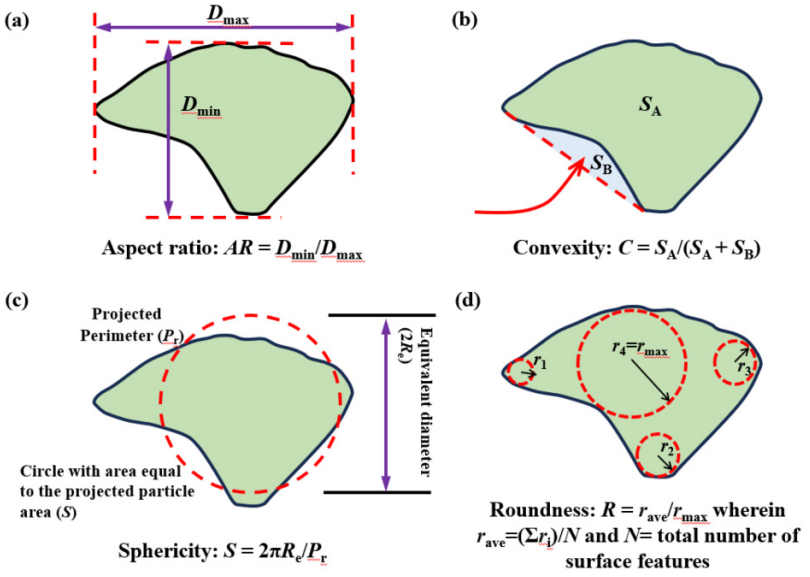

Table 1. Physical properties of tested materials.

Parameter	Round glass bead	Frosted glass bead	Concave glass bead	Convex glass bead	Fujian sand	CDG sand
Specific gravity	2.52	2.52	2.52	2.52	2.65	2.65
Maximum void ratio	0.780	0.761	0.640	1.142	0.884	1.346
Minimum void ratio	0.601	0.577	0.486	0.748	0.512	0.855
Mean grain size (mm)	1.5	1.5	1.5	1.5	1.5	1.5
Uniformity coefficient	1.455	1.455	1.455	1.455	1.455	1.455
Sphericity (2D)	0.954	0.954	0.903	0.888	0.896	0.854
Sphericity (3D)	0.910	0.910	0.840	0.800	0.700	0.720
Aspect ratio (2D)	0.971	0.960	0.712	0.697	0.720	0.686
Aspect ratio (3D)	0.940	0.950	0.620	0.660	0.490	0.60
Convexity (2D)	0.971	0.970	0.948	0.949	0.949	0.925
Convexity (3D)	0.97	0.97	0.94	0.89	0.86	0.80
Roundness (2D)	0.958	0.951	0.689	0.553	0.625	0.543
Root mean square roughness (μm)	1.680	2.408	2.038	2.108	1.815	2.517
Average roughness (μm)	1.445	1.921	1.626	1.680	1.423	1.975

Note: CDG, completely decomposed granite.

After the specimens were isotropically consolidated to the initial stress state of $p' = 100$ kPa (p' is mean effective stress), drained shear tests were performed by increasing q monotonically until failure while α_σ was fixed at the values of 2°, 30°, 45°, 60°, and 88° (see Fig. 5*c*), respectively. To avoid large stress and strain nonuniformities arising in hollow cylinder specimen during shearing, the coefficient of intermediate principal stress b is kept as 0.5 (Cai et al. 2018*a*). During shearing, p', b, and α_σ were kept constant, and q was increased at a rate of 1.5 kPa/min according to Cai et al. (2013, 2018*b*). The standard failure criterion, i.e., $\gamma_g = 5\%$, was widely employed in previous HCTS tests (Miura et al. 1986*a*; Lade et al. 2009). The termination strain of γ_g was thus controlled to be at least greater than 5%. The initial conditions of specimens and detailed test scheme are shown in Table 3.

3. Test results

3.1. Stress–strain behaviors

Figure 6 displays the results of the strain components ε_z, $\gamma_{z\theta}$, ε_r, and ε_θ, in relation to the stress ratio (q/p'). A positive value for ε_z, ε_r, and ε_θ signifies a compressive strain, while a negative one indicates a tensile strain. It is noteworthy that the specimen can achieve a significantly different peak stress ratio under different α_σ. For each material, as q/p' increases, all strain components increase, but the development styles differ and depend significantly on α_σ. Specifically, as α_σ increases from 2° to 88°, ε_z transitions from compression to extension, whereas ε_θ transitions from extension to compression. ε_r is trivially affected by α_σ in the range of $\alpha_\sigma = 0°$–45°, but increases toward the contractive side as α_σ progresses

Fig. 4. Adopted test setup.

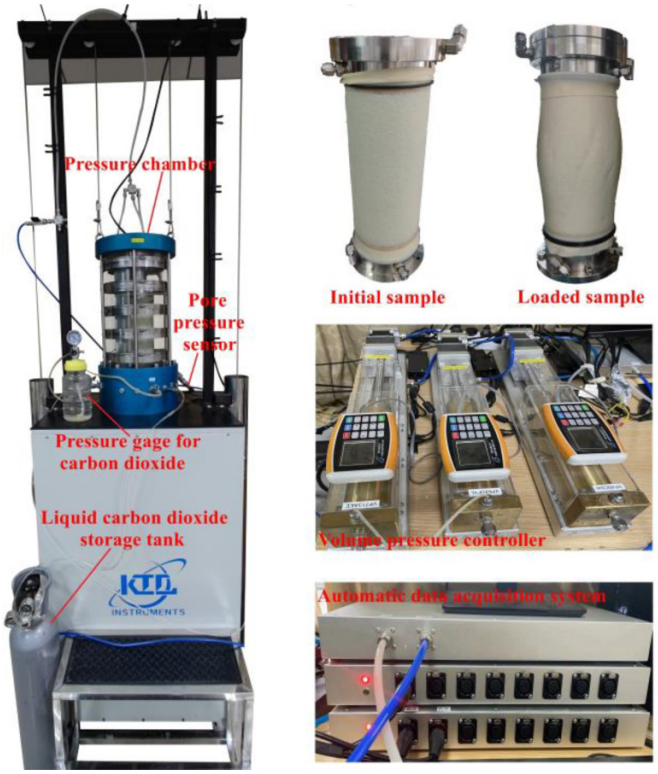

from 45° to 90°. Torsional shear strain $\gamma_{z\theta}$ increases with the increase of α_σ in the range of $\alpha_\sigma = 0°$–45°, and the maximum occurs at $\alpha_\sigma = 45°$, where it becomes a purely torsional shear test.

Figures 7*a* and 7*b* illustrate the typical stress–strain curves using round glass bead and CDG sand as examples. As evident, the peak strength/stress ratio varies with α_σ and exhibits significant strength anisotropy. With the increase of α_σ, the peak strength first decreases and subsequently slightly increases. Notably, the strength of CDG sand, with rough surfaces and irregular particle shapes, varies considerably with changes in α_σ, while the strength of round glass bead varies within a narrow range as α_σ changes, indicating significant dependence of strength anisotropy on particle morphology.

Figures 7*c* and 7*d* compare the stress–strain curves of six granular materials, taking $\alpha_\sigma = 30°$ and 60° as examples. It is evident that as shape irregularity and surface roughness increase, there is a corresponding increase in peak stress ratio. Furthermore, the order of peak stress ratio can be observed as CDG sand > convex glass bead > Fujian sand > concave glass bead > frosted glass bead > round glass bead. CDG sand, possessing the most lower sphericity and aspect ratio as well as the highest surface roughness, exhibits the strongest strength characteristics among the materials. Furthermore, at $\alpha_\sigma = 30°$, the peak strength of frosted glass beads is significantly larger than that of round glass beads. However, this relationship changes at $\alpha_\sigma = 60°$ where the strength of frosted glass beads is similar to that of round glass beads. This suggests that increasing surface roughness contributes to particle friction, which plays a pivotal role in strength under compressive torsion condition. However, it has less effect on strength under tensile torsion condition. Moreover, particle shape appears to have a more substantial impact than surface roughness as even sphere particles (e.g., frosted glass bead) with very high roughness fail to surpass angular/nonspherical particles in terms of strength.

3.2. Strength anisotropy

Even perfectly spherical particles will exhibit slight direction-dependent anisotropy due to stress-induced anisotropy resulting from loading with inclined major principal stress directions. A strength anisotropy factor, i.e., A_η, proposed in existing research was adopted to characterize the direction-dependent strength anisotropy degree (Liu et al. 2022). A_η is defined as the ratio of the maximum stress ratio $(q/p')_{max}$ to the minimum stress ratio $(q/p')_{min}$ under different α_σ, as follows:

$$A_\eta = \frac{(q/p')_{max}}{(q/p')_{min}} \quad (4)$$

A larger A_η value corresponds to a greater disparity between the maximum and minimum peak strengths under different α_σ, indicating a higher degree of strength anisotropy. Figure 8*a* summarizes the peak stress ratios of the tested six materials under different α_σ, while Fig. 8*b* displays the corresponding A_η for these six granular materials. It is noteworthy that in Fig. 8*a*, materials containing spherical particles (e.g., round and frosted glass bead) exhibit a narrow range of strength variation under varying α_σ, i.e., a low strength anisotropy, while particles with irregular shapes (e.g., convex glass bead, Fujian sand, and CDG sand) have significant strength anisotropy. Granular materials with irregular shapes possess higher peak strengths when subjected to a vertical major principal stress axis. However, their peak strengths exhibited a significantly greater variation with α_σ in comparison to granular materials with spherical shapes. As seen in Fig. 7, CDG sand demonstrates lower normal stiffness and greater susceptibility to deformation during the initial shear stage compared to other materials, a finding consistent with previous studies by Li et al. (2019) and Sandeep et al. (2022). Despite its more irregular particle shape, the A_η value for CDG sand, which possesses a larger void ratio and deformability, is marginally lower than that of Fujian sand and convex glass beads. As depicted in Fig. 10*h*, the volumetric contraction of CDG sand at $\alpha_\sigma = 60°$ is considerably more pronounced than that at $\alpha_\sigma = 2°$, with this increase being significantly more substantial than in other materials. This heightened densification at $\alpha_\sigma = 60°$, where the minimum peak strength of CDG sand is observed, may potentially contribute to a decrease in the A_η values. Note that the findings presented in Fig. 8 emphasize the reliance of strength anisotropy on particle shape. For an in-depth understanding of how relative density and mean effective stress influence the magnitude of strength anisotropy, one can refer to the studies by Yoshimine et al. (1998), Cai (2010), and Yang et al. (2016). Figure 9 illustrates the relationship between A_η and various shape indicators. As S, R, AR, and C decrease, a general increase in A_η is observed. This implies that the direction-

Fig. 5. Illustrations for stress paths for tests with fixed principal stress axes: (*a*) stress states of soil elements in sloping ground; (*b*) stress and strain states in hollow cylinder apparatus; (*c*) stress paths of this study; and (*d*) definitions for noncoaxiality angle.

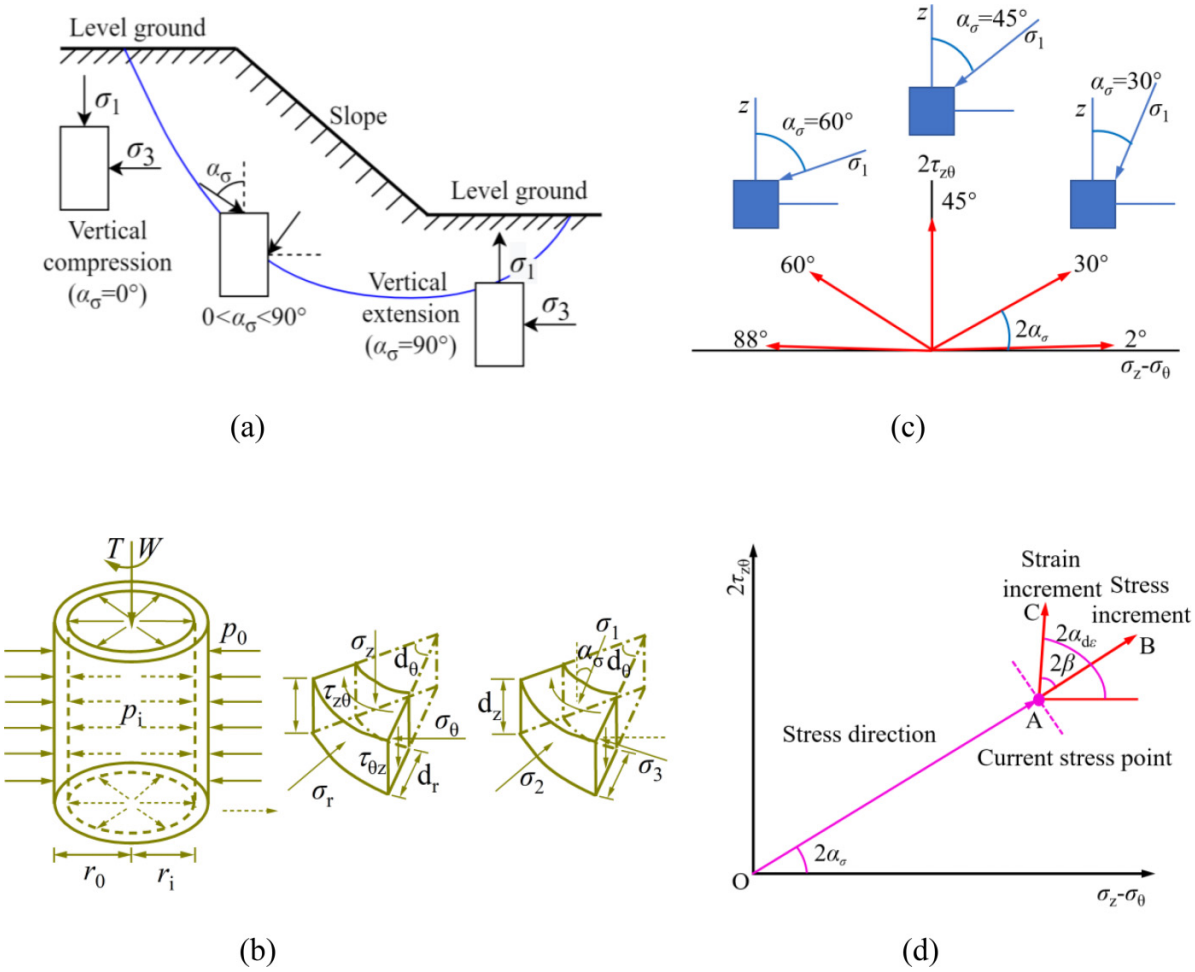

Table 2. Equations for calculating stresses and strains.

	Stress	Strain
Vertical	$\sigma_z = \frac{W}{\pi(r_0^2-r_i^2)} + \frac{p_0 r_0^2 - p_i r_i^2}{r_0^2-r_i^2}$	$\varepsilon_z = \frac{z}{H}$
Radial	$\sigma_r = \frac{p_0 r_0 + p_i r_i}{r_0+r_i}$	$\varepsilon_r = -\frac{u_0-u_i}{r_0-r_i}$
Circumferential	$\sigma_0 = \frac{p_0 r_0 - p_i r_i}{r_0-r_i}$	$\varepsilon_0 = -\frac{u_0+u_i}{r_0+r_i}$
Shear	$\tau_{z\theta} = \frac{3T}{2\pi(r_0^3-r_i^3)}$	$\gamma_{z\theta} = \frac{2\theta(r_0^3-r_i^3)}{3H(r_0^2-r_i^2)}$
Major principal	$\sigma_1 = \frac{\sigma_z+\sigma_\theta}{2} + \sqrt{\left(\frac{\sigma_z-\sigma_\theta}{2}\right)^2 + \tau_{z\theta}^2}$	$\varepsilon_1 = \frac{\varepsilon_z+\varepsilon_\theta}{2} + \sqrt{\left(\frac{\varepsilon_z-\varepsilon_\theta}{2}\right)^2 + \left(\frac{\gamma_{z\theta}}{2}\right)^2}$
Intermediate principal	$\sigma_2 = \sigma_r$	$\varepsilon_2 = \varepsilon_r$
Minor principal	$\sigma_3 = \frac{\sigma_z+\sigma_\theta}{2} - \sqrt{\left(\frac{\sigma_z-\sigma_\theta}{2}\right)^2 + \tau_{z\theta}^2}$	$\varepsilon_3 = \frac{\varepsilon_z+\varepsilon_\theta}{2} \sqrt{\left(\frac{\varepsilon_z-\varepsilon_\theta}{2}\right)^2 + \left(\frac{\gamma_{z\theta}}{2}\right)^2}$
Deviatoric	$q = \sqrt{\frac{1}{2}\left[(\sigma_1-\sigma_2)^2 + (\sigma_2-\sigma_3)^2 + (\sigma_3-\sigma_1)^2\right]}$	$\gamma_g = \sqrt{\frac{2}{9}\left[(\varepsilon_1-\varepsilon_2)^2 + (\varepsilon_2-\varepsilon_3)^2 + (\varepsilon_3-\varepsilon_1)^2\right]}$

dependent anisotropy heavily relies on the morphology of the particles, and it becomes more prominent with an increasing irregularity in particle shape.

3.3. Stress–dilatancy behavior

Figures 10*a*–10*f* illustrate the relationship between volumetric strain ε_v and stress ratio q/p'. It is evident that all samples undergo initial contraction, followed by dilation, with an increase in q/p' under various α_σ. Generally, the contractive ε_v increases as α_σ approaches approximately 45°, and decreases with a further increase in α_σ, indicating a high dependence of ε_v on α_σ. The phase transformation state (PTS) point has been added in Figs. 10*a*–10*f*, which represents the characteristic state at which a sample undergoes a transition from

Table 3. Test program.

Material	α_σ (°)	B	p' (kPa)	D_r (%)
Round glass bead	2	0.5	100	88.5
	30			89.1
	45			89.7
	60			89.6
	88			88.5
Frosted glass bead	2	0.5	100	87.6
	30			87.1
	45			89.3
	60			88.7
	88			88.2
Concave glass bead	2	0.5	100	85.7
	30			87.0
	45			85.7
	60			87.0
	88			86.4
Convex glass bead	2	0.5	100	85.5
	30			85.3
	45			85.8
	60			86.0
	88			85.8
Fujian sand	2	0.5	100	86.3
	30			86.0
	45			86.6
	60			86.3
	88			85.8
CDG sand	2	0.5	100	85.7
	30			86.1
	45			85.9
	60			85.5
	88			85.3

Note: CDG, completely decomposed granite.

contraction to dilation during drained tests. As shown in Figs. 10*a*–10*f*, for round and frosted glass beads with spherical particle shapes, the value of q/p' corresponding to the PTS point is roughly the same for varying α_σ. However, for the concave and convex glass beads as well as Fujian and CDG sands, the q/p' value corresponding to the PTS point varies significantly and exhibits a general decreasing trend with the increase of α_σ. This implies that the distinct initial fabric resulting from the particle morphology has substantial influence on PTS under different α_σ in drained tests. More irregular particle shape tends to exhibit a stronger anisotropy in volumetric strain response in terms of PTS.

Figures 10*g*–10*h* compare the ε_v versus q/p' of six granular materials under $\alpha_\sigma = 30^\circ$ and 60°. It is evident that particle morphology significantly impacts volumetric strain. Specifically, the round, frosted, and concave glass beads with smaller index void ratios exhibit a significantly lower contractive ε_v than the convex glass bead and CDG sand with larger index void ratios. Furthermore, materials with irregular particle shape and high strength exhibit a larger stress ratio at the PTS point.

In Fig. 11, the stress–dilatancy relationship under different α_σ is demonstrated by presenting the dilatancy ratio ($d\varepsilon_v/d\gamma_g$) versus q/p'. It is clear that regardless of materials, the stress–dilatancy relationship in the early stage of shearing significantly changes with varying α_σ. For instance, for round and frosted glass beads with spherical shape, there is a general increase in $d\varepsilon_v/d\gamma_g$ with an increase in α_σ in the early stages of shearing under the same q/p'. The stress–dilatancy relationship for these two materials under different α_σ at the end of shearing, however, basically converges to a unique line. For concave glass beads, convex glass beads, Fujian sand, and CDG sand with angular shapes, the $d\varepsilon_v/d\gamma_g$ roughly reduces with an increase in α_σ in the early stage of shearing under the same q/p'. Furthermore, in the later stage of shearing, although the samples have a much similar void ratio or state parameter, an increase in α_σ significantly reduces the corresponding q/p' at PTS points, highlighting a strong dependency of q/p' at PTS points on α_σ. Figures 10 and 11 indicate that the influence of particle morphology and preferential rearrangement direction of particles at different α_σ on the stress–dilatancy is complex. Therefore, future research should focus on establishing a more comprehensive flow rule that reflects the impact of internal fabric of granular packings on stress–dilatancy behavior. Furthermore, Figs. 10 and 11 demonstrate the behavior of dense granular materials in terms of volumetric strain under different principal stress directions. Lower relative density and mean effective stress potentially lead to a more contractive volumetric strain behavior in granular materials. However, the potential impact of these changes in dilatancy on the sensitivity of volumetric strain to α_σ remains an open question, warranting in-depth investigation in future research effort.

4. Interplay between anisotropic behavior and microstructure

4.1. Microstructure quantification procedure based on CT

To gain a comprehensive understanding of macroscopic behavior, it is crucial to investigate the internal fabric of particle assembly. To capture the initial fabric of particle packings, X-ray tomography scans were conducted on six particle assemblies using the Nikon XT H225ST 2X Computed Tomography system at PolyU. This advanced synchrotron X-ray microtomography facility provides a powerful X-ray beam with a wide range of intensities, ranging from 20 to 225 W. Such a broad energy spectrum enables versatile imaging capabilities and allows for the examination of materials with diverse compositions and densities. The X-ray system comprises an X-ray beam tube (or source), a high voltage generator, a sample manipulator, and a flat panel detector. Six types of granular materials were prepared by dry tamping method into cylindrical specimens with a diameter of 24.5 mm and a height of 52 mm, which were proportionally equivalent to the hollow cylindrical specimens. The dimensions of these cylindrical specimens are ample enough to facilitate a specimen preparation technique akin to the original hollow cylindrical specimens. Consequently, the unifor-

Fig. 6. Various strain components (i.e., ε_z, ε_θ, ε_r, and $\gamma_{z\theta}$) versus q/p' for (*a*) round glass bead; (*b*) frosted glass bead; (*c*) concave glass bead; (*d*) convex glass bead; (*e*) Fujian sand; and (*f*) completely decomposed granite sand.

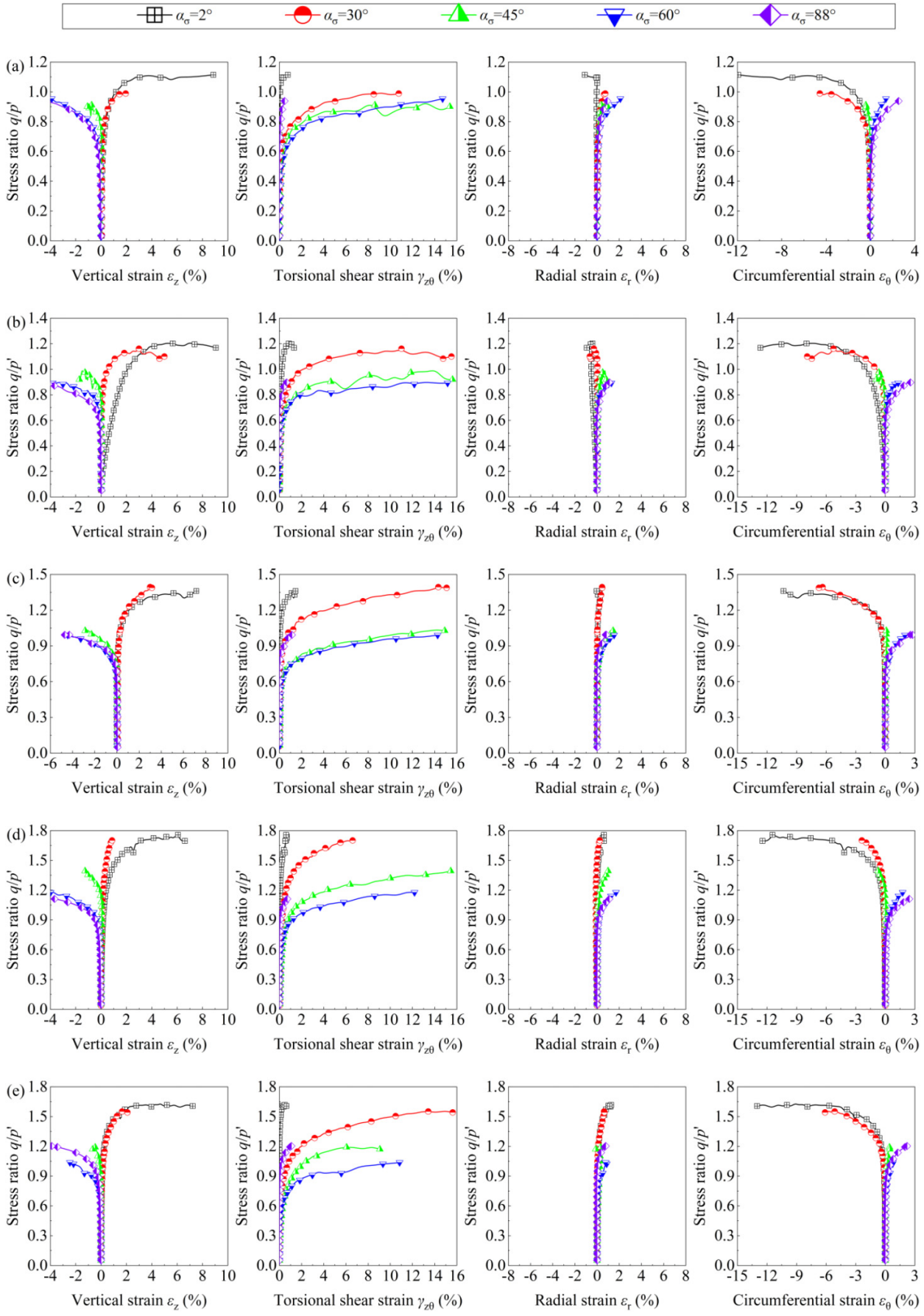

Fig. 6. (*concluded*).

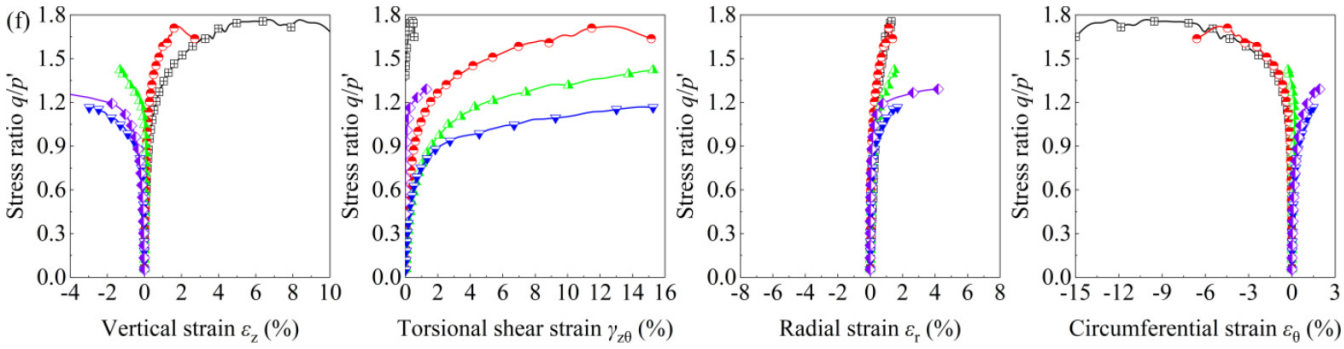

Fig. 7. Comparisons of stress–strain curves for (*a*) round glass bead; (*b*) completely decomposed granite (CDG) sand; (*c*) $\alpha_\sigma = 30°$; and (*d*) $\alpha_\sigma = 60°$.

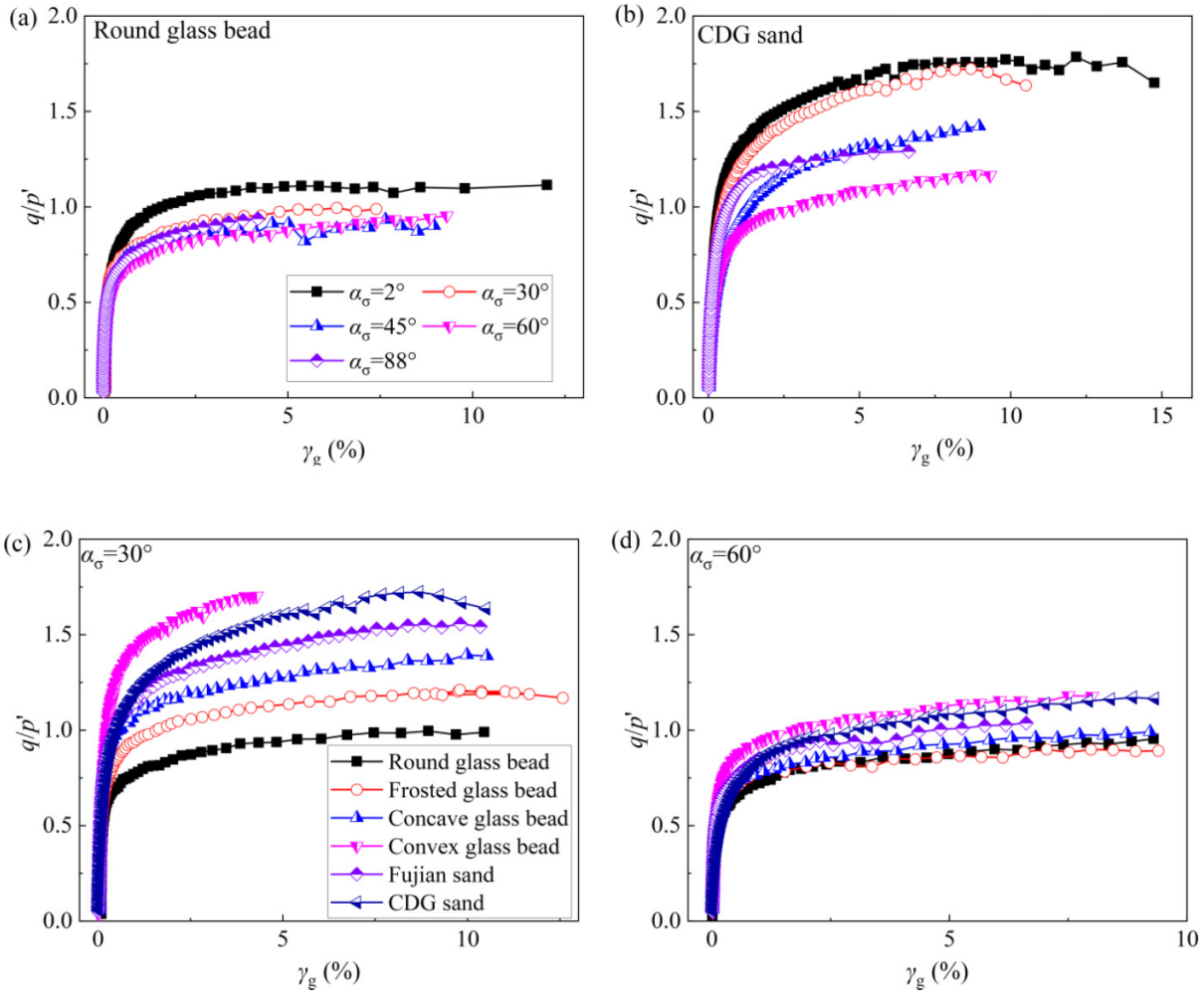

mity of the CT-scanned specimens and the arrangement of particles can be considered analogous to that of the original hollow cylindrical specimens. The X-rays penetrate through the sample, creating a shadow image that is captured by the flat panel detector. During the scanning process, the samples were placed on a manipulator stage, which allowed for rotation. For each sample, a total of 3000 projections were collected as the sample underwent a 360° rotation. Subsequently, an average of 2000 images were obtained for each sample during the complete 360° rotation, with a pixel size of 25 μm.

Prior to reconstructing the geometry of 3D particles, median and Gaussian filter techniques were employed to reduce image noise. Subsequently, thresholding was applied to convert the raw image into a binarized form, with background represented as 0 and grains represented as 1. The 3D watershed algorithm was then utilized to segment the individual grains, assigning different colors and labels to each grain. For

Fig. 8. Strength anisotropy under different α_σs: (*a*) q/p' versus α_σ and (*b*) A_η versus particle shape factor. CDG, completely decomposed granite.

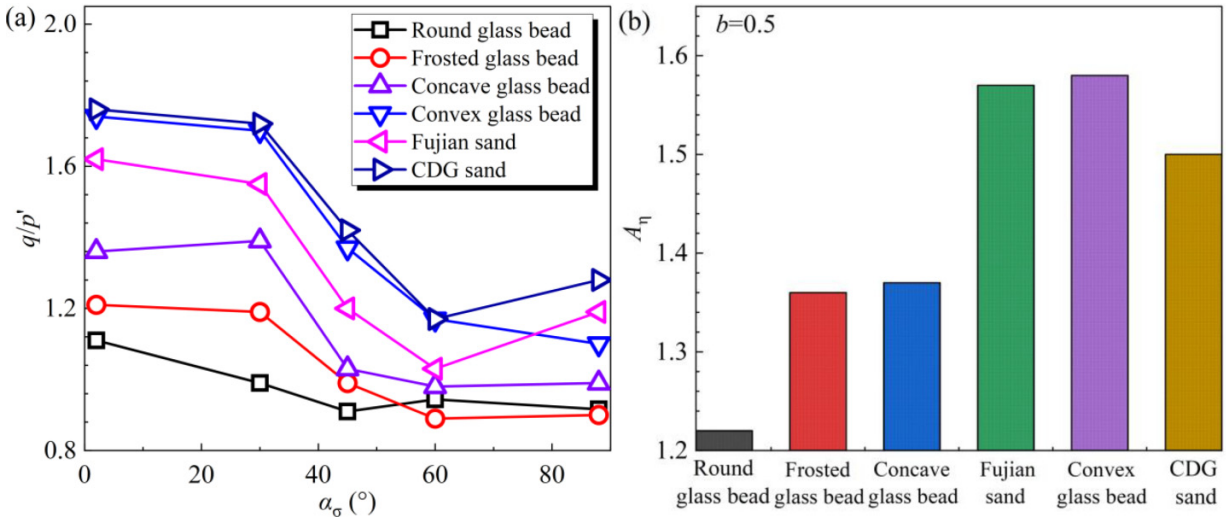

Fig. 9. Relationship between A_η and various morphological factors. AR, aspect ratio; CDG, completely decomposed granite.

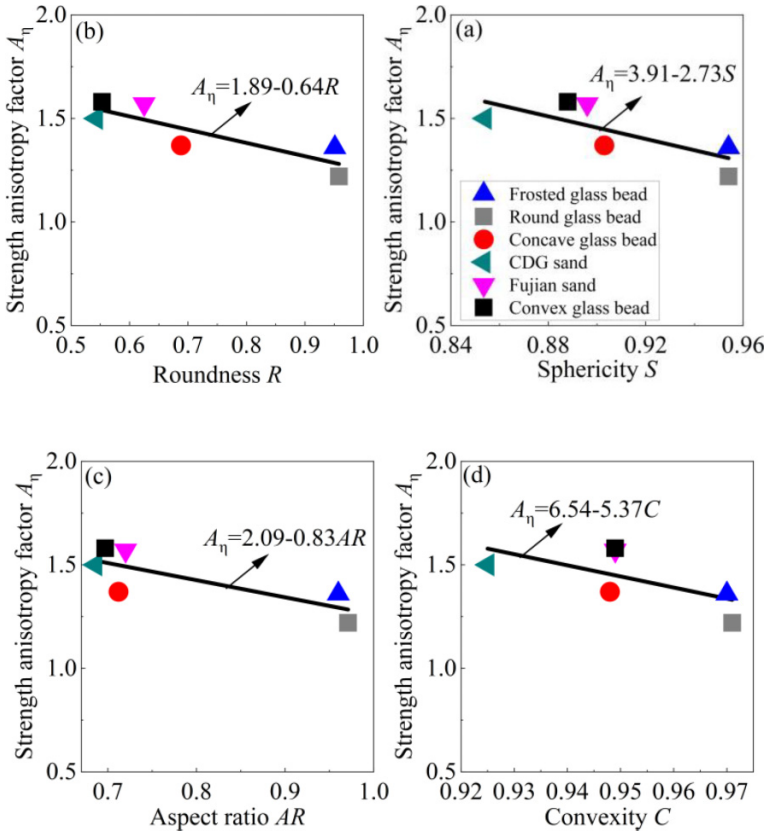

better visualization and evaluation of the grains' morphological features, the marching cube algorithm was adopted to smoothly convert the grain surface into triangle meshes. Figure 12*a* illustrates a typical original cross-section captured by CT, followed by images after noise removal (Fig. 12*b*) and watershed processing (Fig. 12*c*), using Fujian sand as an example. Figures 12*d* and 12*e* showcase a typical 3D reconstruction of two cylindrical particle packings, exemplified by concave and convex glass beads. Figure 12*f* presents a standard schematic diagram used for determining the orientation of the particle's primary axis. The black lines within the diagram symbolize the direction of the particle's main axis. In Fig. 12*g*, the angles between the major axis and the *x*, *y*, and *z* axes, donated as φ_x, φ_y, and φ_z, are depicted. Additionally, the angle between the major axis orientation and the horizontal plane (i.e., *x*–*y* plane), referred to as φ_H, can be derived using φ_z. The detailed methodology for deriving the orientation of the particle's major axis is elucidated in the Appendix A.

Fig. 10. Volumetric strain ε_v versus stress ratio q/p' for (*a*) round glass bead; (*b*) frosted glass bead; (*c*) concave glass bead; (*d*) convex glass bead; (*e*) Fujian sand; (*f*) completely decomposed granite (CDG) sand; (*g*) $\alpha_\sigma = 30°$; and (*h*) $\alpha_\sigma = 60°$.

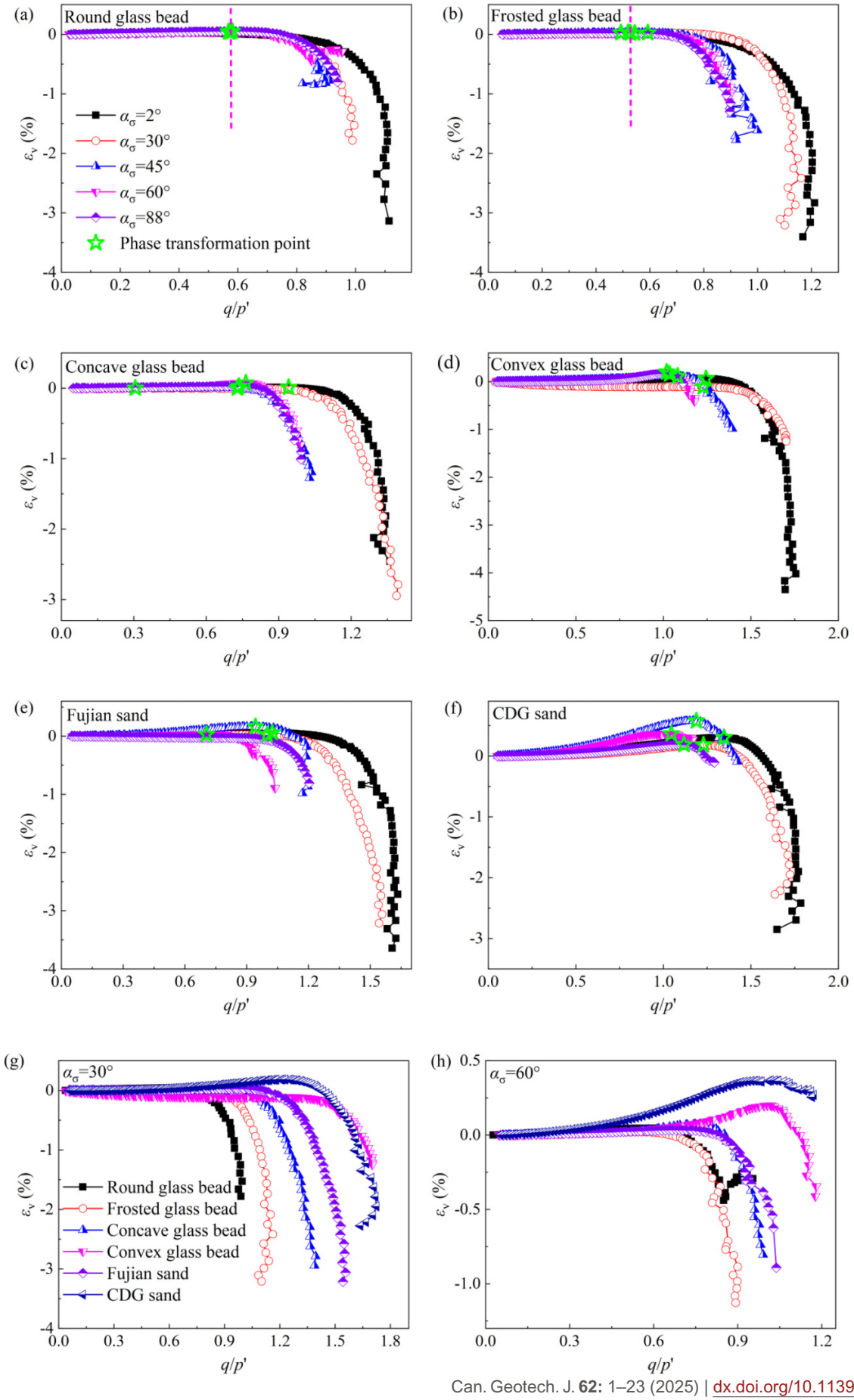

Fig. 11. Stress–dilatancy relationships under different α_σ. CDG, completely decomposed granite.

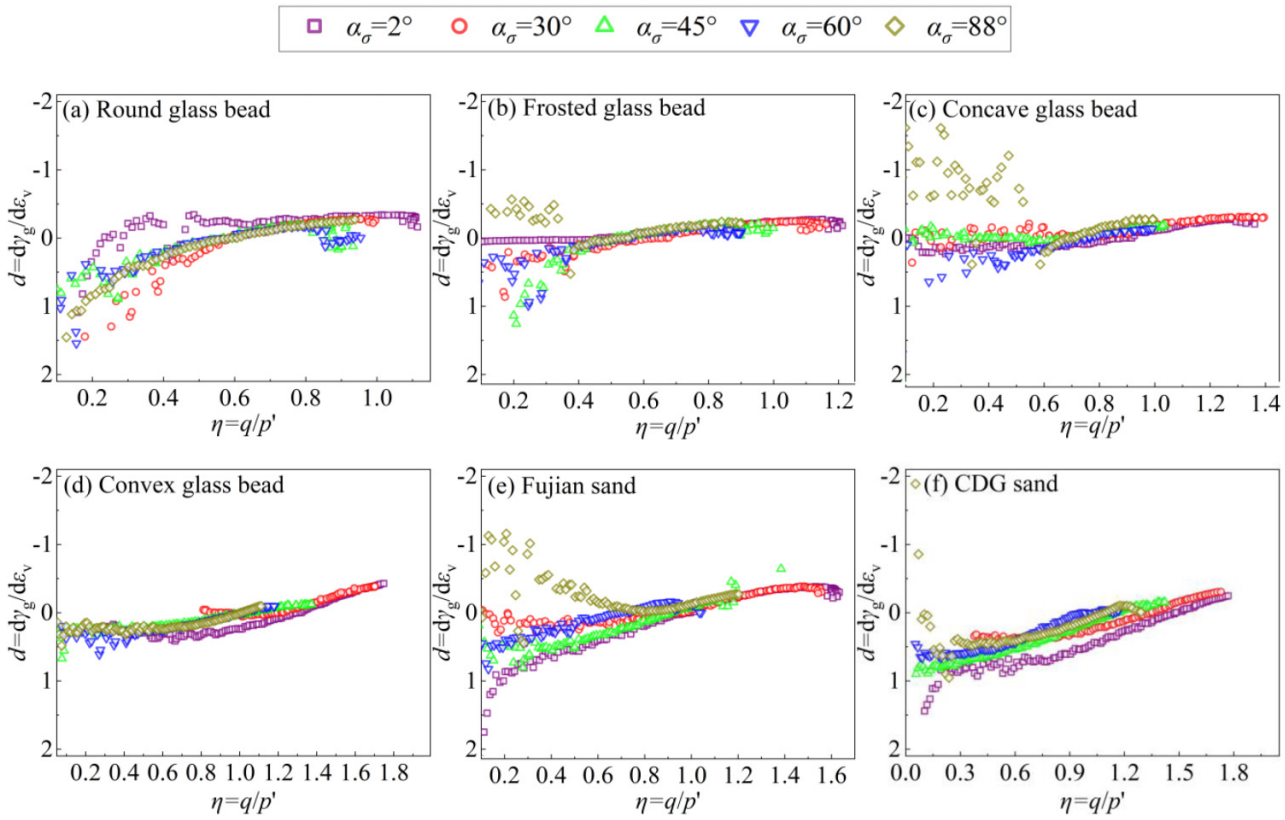

4.2. Role of particle morphology in microscopic fabric anisotropy

The initial particle orientation/arrangement is analyzed in four nonspherical granular packings, namely concave glass bead, convex glass bead, Fujian sand, and CDG sand. In the spherical granular packings consisting of round and frosted glass beads, each particle's diameter serves as the major axis, allowing for orientation in all directions. Hence, the particle packing can be deemed to be isotropic. However, in CT measurements, there might be a specific major axis and orientation for round and frosted glass beads caused by slight protrusions on the particle surface, which complicates accurate matching with the actual situation. As a result, the analysis of particle orientation in spherical particle packings with highly isotropic fabric is not conducted here. Figures 13*a*–13*c* depict φ_x, φ_y, and φ_z for the four materials. φ_x, φ_y, and φ_z represent the angles between the major axis of the particles and the x, y, and z axes, respectively. It is evident that the particle shape significantly influences the initial internal arrangement of the particle packing. The distribution of φ_x, φ_y, and φ_z in the four materials spans from 0° to 180°, signifying a certain level of randomness in the particle orientation. Among the four materials examined, the concave glass beads, characterized by their highly uniform particle shape (i.e., exhibiting relatively large S, R, C, and AR), exhibit a more concentrated preferred orientation of the major axis concerning the x, y, and z axes following the initial deposition process. In contrast, the other three materials demonstrate a broader range of preferred orientations of their major axes concerning the x, y, and z axes, indicating a more anisotropic fabric. This implies that the increase in irregularity of particle shape will impact the arrangement and contact among particles, resulting in a greater enrichment of particle orientation.

The angle between the orientation of the particle's major axis and the horizontal/bedding plane (φ_H, Fig. 13*d*) can describe the cross-anisotropy degree of the sand inter-structure, holding particular importance in the mechanical analysis of the specimens under various major principal stress directions. It is evident from Fig. 13*d* that the particle orientation in all four samples prepared utilizing the dry tamping method is primarily horizontal (perpendicular to the z axis). The concave glass beads, with their more regular shape compared to the other materials, tend to exhibit a closer alignment to the horizontal plane. However, for packings consisting of particles with more complex shapes (e.g., convex glass beads, CDG, and Fujian sands), the angle between particle orientation and the horizontal plane becomes more random.

A random arrangement of nonspherical particles exhibits statistical properties in both the spatial arrangement of the particles and the corresponding voids. Curray (1956) proposed the vector magnitude Δ as a measure to quantify the degree of anisotropy in the preferred particle orientation. The index Δ, typically derived from φ_H, can be expressed as

Fig. 12. Typical computed tomography cross-sections of Fujian sand: (*a*) original; (*b*) after noise removal; and (*c*) after watershed processing; reconstruction for (*d*) concave glass bead and (*e*) convex glass bead; schematics for (*f*) particle orientation determination and (*g*) angles between major axis with *x*–*y* plane, *x*, *y*, and *z* axes.

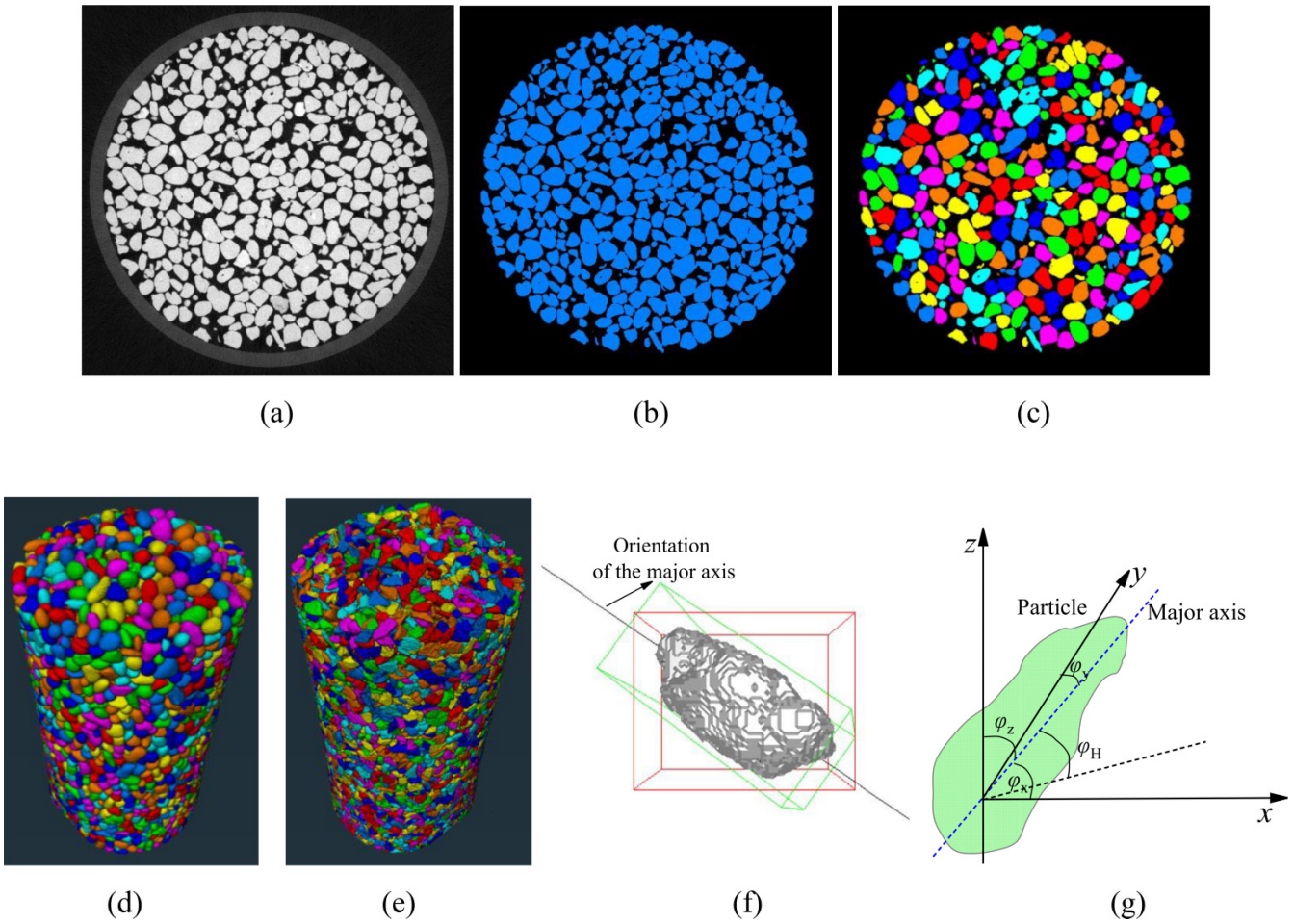

follows:

$$\Delta = \frac{1}{2N}\sqrt{\left(\sum_{k=1}^{2N}\cos 2\varphi_{\mathrm{H}}\right)^2 + \left(\sum_{k=1}^{2N}\sin 2\varphi_{\mathrm{H}}\right)^2} \quad (5)$$

where φ_{H} represents the inclination angle of the *k*th unit vector *n*, measured with respect to the horizontal plane *x*–*y*. The magnitude of Δ is influenced by both the particle shape and the process of deposition. It ranges from zero, signifying isotropic material fabric, to unity, implying that the major axes of all particles are uniformly distributed in the horizontal plane *x*–*y*. A higher value of Δ indicates a greater level of anisotropy and complexity in the fabric.

Figure 14 illustrates the correlation between various morphological factors and Δ. Note that in Fig. 14, when considering *S*, *R*, AR, and $C = 1$, it represents spherical particles with an isotropic fabric and $\Delta = 0$. It can be observed that *S*, *R*, and AR all significantly influence Δ, and there exists a strong negative relationship with Δ, as follows:

$$\Delta = 3.14 - 3.11S \left(R^2 = 0.87\right) \quad (6)$$

$$\Delta = 0.97 - 0.95R \left(R^2 = 0.95\right) \quad (7)$$

$$\Delta = 1.35 - 1.34\mathrm{AR} \left(R^2 = 0.96\right) \quad (8)$$

As *S*, *R*, and AR decrease, Δ significantly increases, indicating that a higher irregularity in particle shape results in a stronger fabric anisotropy within the particle packing. In Fig. 14*d*, the influence of *C* on Δ is less significant compared to the other indices.

4.3. Interplay between strength anisotropy and fabric anisotropy

Comprehending the interplay between particle arrangement anisotropy/fabric and direction-dependent strength anisotropy is essential for accurate modeling and prediction of the behavior of granular materials under complex loading conditions. A mixture of spherical particles tends to self-arrange into an isotropic structure, leading to homogeneous mechanical properties. However, when particles are angular and preferentially oriented, anisotropy in the material's strength emerges. This anisotropy is a consequence of the asymmetry in the distribution of stress-carrying paths within the material. It is well-known that dry tamping method pro-

Fig. 13. Particle orientation angle of various materials with respect to (*a*) *z* axis; (*b*) *x* axis; (*c*) *y* axis; and (*d*) *x*–*y* plane. CDG, completely decomposed granite.

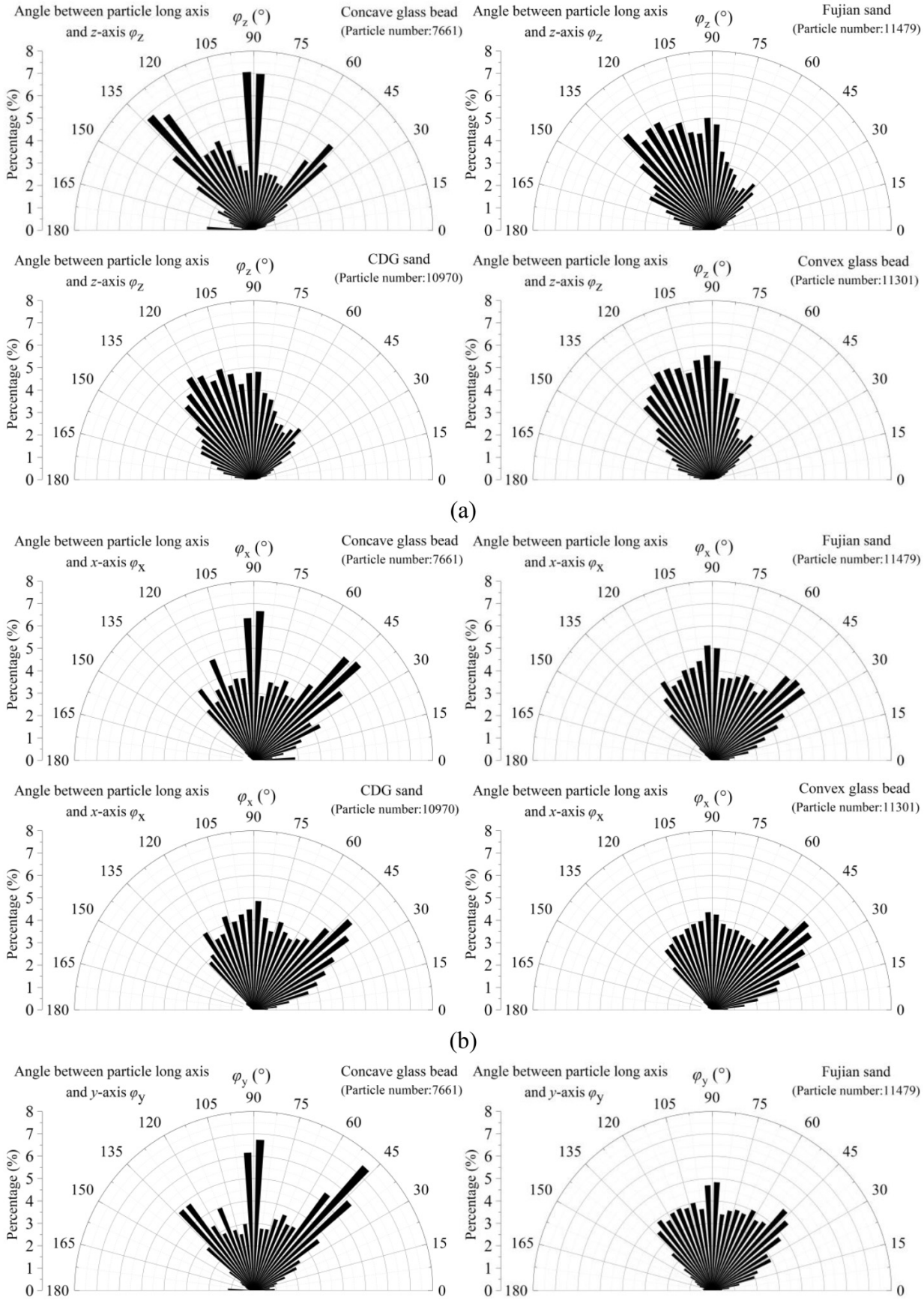

Fig. 13. (*concluded*).

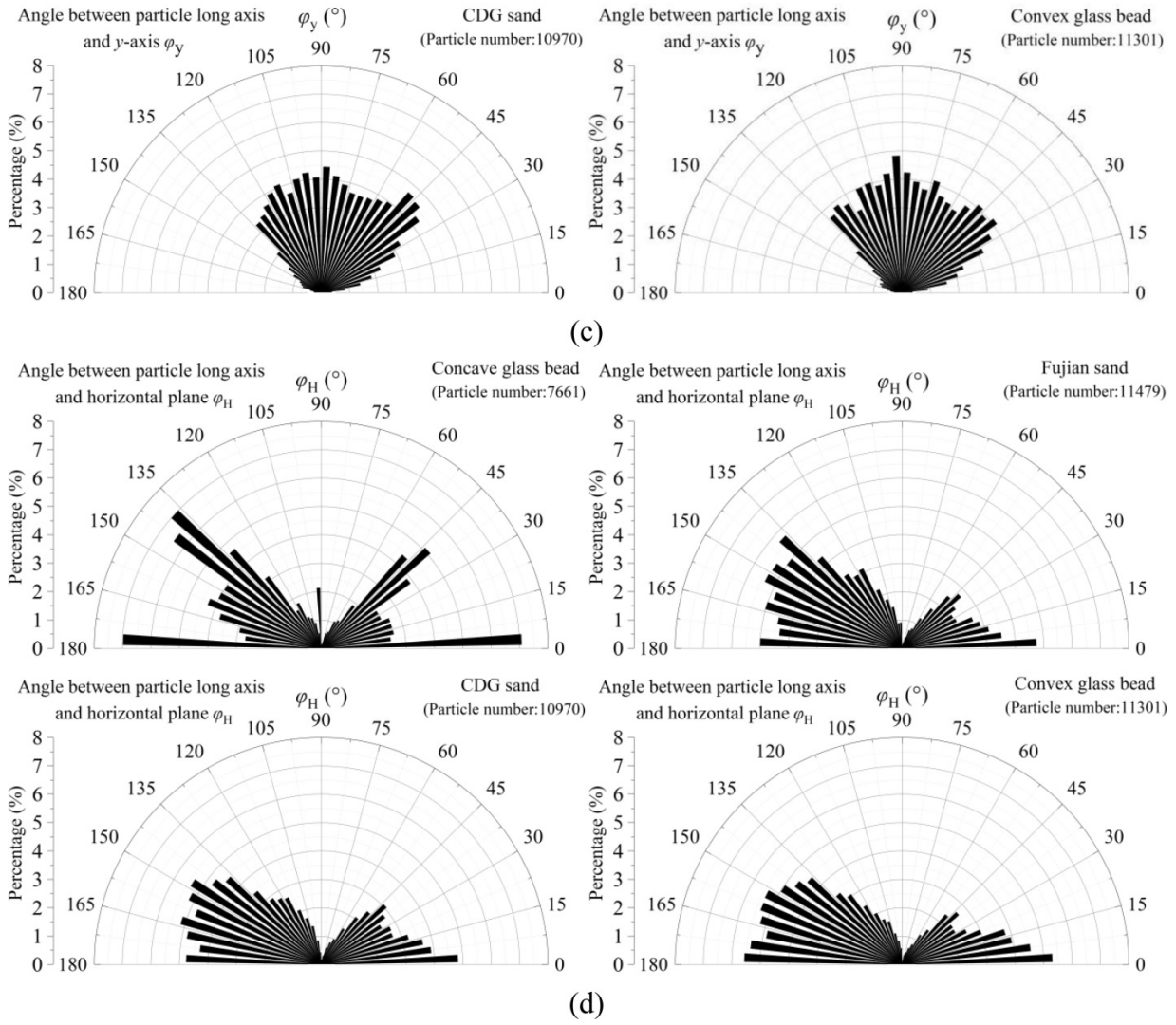

duces a cross-anisotropic soil structure consisting of a deposition direction and a bedding plane (Zamanian et al. 2021). Therefore, the vertical direction of the packing is densely packed and expected to possess maximum resistance due to the strong particle interlocking, while the horizontal bedding plane is the weakest with low stability and high deformation due to its propensity to rotate under torque generated from eccentric forces, as depicted in Fig. 15*a*. When the principal stress angle changes, the contribution of various stress-carrying paths alters. When the principal stress angle is aligned parallel to the particle alignment, the axial path carries the majority of the stress, resulting in the highest strength. Conversely, when the principal stress angle is perpendicular to the particle alignment, the transverse path becomes dominant, leading to a lower strength. Therefore, the material fabric/particle oretation plays a vital role in determining the overall strength and strength anisotropy of material under different α_σ.

Figure 15*b* illustrates the correlation between Δ, which represents the initial structural fabric anisotropy, and A_η, which quantifies the strength anisotropy. It should be noted that in Fig. 15*b*, complete isotropic stacking is considered as having no strength anisotropy (i.e., $\Delta = 1$). As Δ increases, A_η increases and eventually stabilizes once Δ surpasses a certain threshold value. This evidence suggests a close relationship between strength anisotropy and initial fabric anisotropy. Changes in preferred alignment of particles due to different particle shapes can lead to varying degrees of anisotropy, causing the material's strength properties to differ significantly depending on the direction of the applied stress. It is clear that an increase in fabric anisotropy caused by particle shape alterations tends to induce a greater degree of strength anisotropy in particle packing. To some extent, the essential mechanism of macroscopic strength anisotropy can be attributed to the microstructure's anisotropy. The relationship between A_η and Δ can be approximated as follows:

$$(9)\quad \begin{cases} A_\eta = 1 + 2.44\Delta^{1.72} (0.41 \geq \Delta \geq 0) \\ A_\eta \approx 1.58 (\Delta \geq 0.41) \end{cases}$$

Note that the connections identified in this study between particle shape and fabric anisotropy, as well as between fab-

Fig. 14. Relationship between Δ and various morphological factors. CDG, completely decomposed granite.

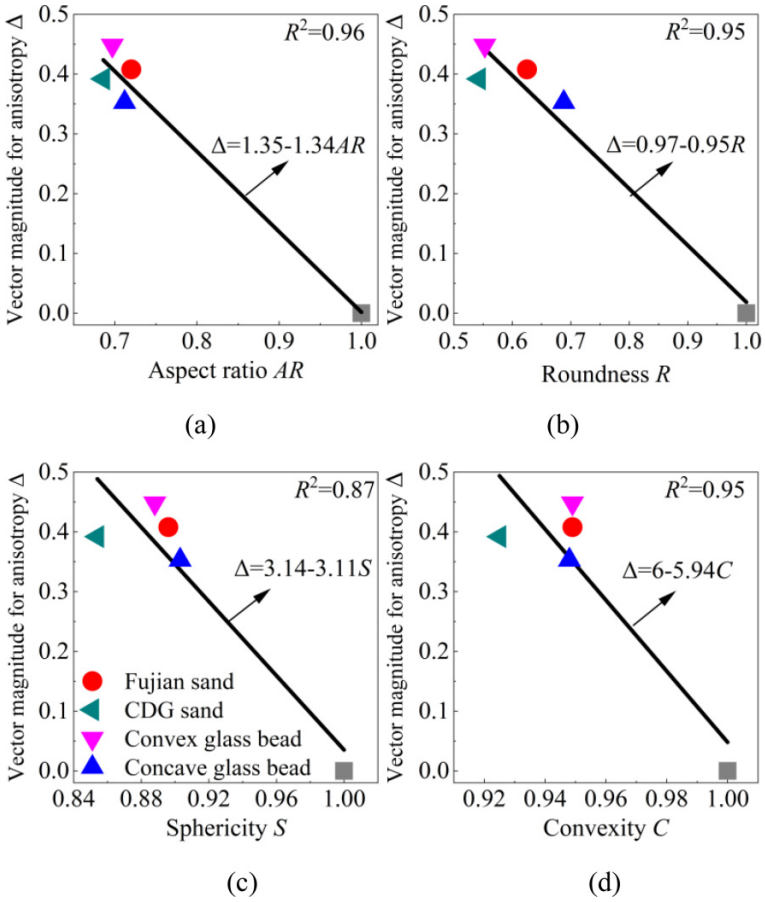

Fig. 15. Schematic for anisotropy: (*a*) structure of cross-anisotropic deposited sands (modified after Miura et al. (1986*a*)) and (*b*) correlation between A_η and Δ. CDG, completely decomposed granite.

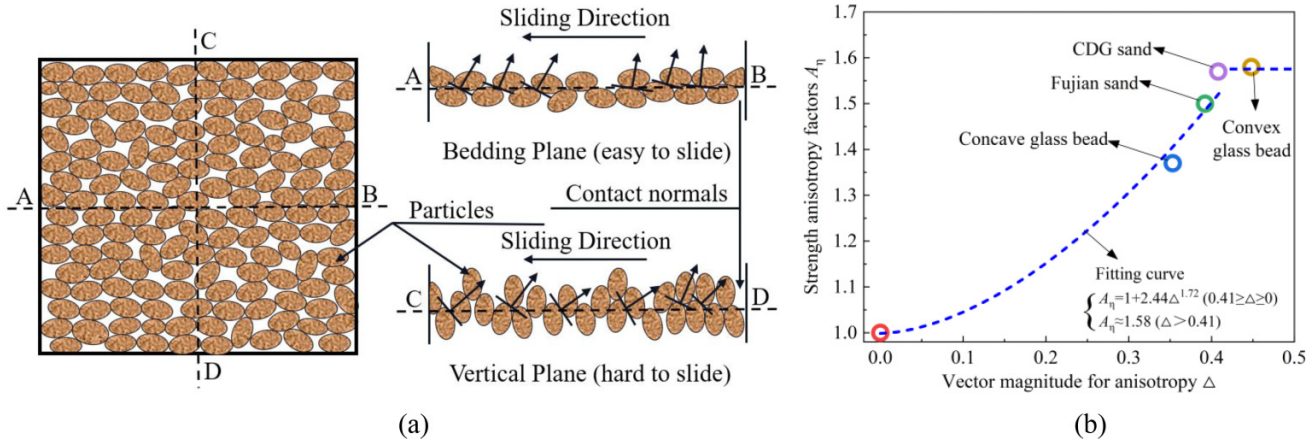

ric anisotropy and strength anisotropy, are derived from test data on dense specimens. These findings hold practical significance for backfill engineering projects involving densely packed foundation soil, such as embankments. Nonetheless, the precise impact of relative density and mean effective stress on the anisotropy of strength and fabric, as well as their specific effects on eqs. 6–9, remains obscure. It would be beneficial for future studies to encompass a wider array of relative densities and mean effective stress levels to elucidate these interactions further.

5. Anisotropic failure criterion

Proper characterization of strength anisotropy in soils requires a suitable anisotropic failure criterion. As mentioned before, the strength of soil depends on how the loading is

applied with respect to the bedding plane of soils. Consequently, it is crucial to accurately quantify the relative orientation between the stress direction and material fabric to predict the behavior of strength anisotropy. The first joint invariant, A, can adequately represent the relationship between stress direction and material fabric in 3D space, and can also describe the impact of inherent anisotropy on sand behavior (Dafalias et al. 2004; Gao and Zhao 2012). The formula for A, under typical conditions of a hollow cylindrical torsional shear test, is presented in eq. 11, with further details provided in the Appendix B.

$$A = \frac{-3\cos^2\alpha_\sigma + (b+1)}{2\sqrt{b^2 - b + 1}} \quad (10)$$

We develop an anisotropic failure criterion for granular soils by incorporating Δ and A in the generalization of the failure criterion in Lade (1977), as follows:

$$f = \left(\frac{I_1^3}{I_3} - 27\right)\left(\frac{I_1}{p_a}\right)^m = \eta_r \exp\left[g(A, \Delta)\right] + \zeta \quad (11)$$

where m, η_r, and ζ are model parameters; p_a=100 kPa; I_1 ($=\sigma_1 + \sigma_2 + \sigma_3$) and $I_3 = \sigma_1\sigma_2\sigma_3$ are the first and third invariants. The form of anisotropic interpolation function for $g(A, \Delta)$ is provided in Appendix B. Δ is vector magnitude with the range of $0 < \Delta \leq 1$. It should be noted that the round and frosted glass beads utilized in this study are not perfectly spherical particles, as evidenced by the measured values of S, R, AR, and C (see Table 1), which is not equal to 1, and they possess a moderate degree of strength anisotropy. In the case of round and frosted glass beads with a nearly spherical shape and isotropic structure, Δ is small and challenging to determine through CT measurements. Therefore, the values of Δ for round and frosted glass beads are calculated using eqs. 6–8 and are determined to be 0.094 and 0.101, respectively. The $p = 100$ kPa was constant in all tests; m will not affect results and, consequently, it was not considered in parameter calibrations.

To calibrate the parameters, the test data were plotted in the $(I_1^3/I_3 - 27)$–A space as shown in Fig. 16*a*. By conducting a regressive and fitting analysis on eq. 11, the best-fit model parameters for each material were obtained and presented in Fig. 16*a*. The comparison between the interpolation of results for q/p' with measured q/p' is demonstrated in Fig. 16*b*. Moreover, the fitted strength envelope in $(\sigma_z - \sigma_\theta)$–$2\tau_{z\theta}$ plane was depicted in Fig. 16*c* for all materials. As evident in Figs. 16*b* and 16*c*, the fitting results of the peak q/p' align with the test data, and the anisotropic failure criterion can well approximate the strength envelope. The anisotropic failure criterion proposed in this study is proved to be suitable for describing the strength failure envelope of granular materials with diverse shapes and may serve as an efficient analysis tool in practical engineering applications. Additionally, the direction of major principal strain increment is demonstrated in Fig. 16*c*. As observed, noncoaxiality is more prominent in the early stages of loading, but stabilizes gradually in the later stages of loading.

6. Conclusions

An experimental program utilizing HCA was conducted to investigate how particle morphology affected the mechanical anisotropy of granular materials. The program involved 30 monotonic drained HCTA tests on six granular materials with distinct particle morphologies under various orientations of major principal stress axis. Precise measurements of particle morphological indices were also performed for each material. Furthermore, X-ray microtomography was utilized to obtain high-resolution 3D images of the particle packing, providing insights into the microscopic mechanism of mechanical anisotropy via internal fabric/particle orientation.

HCA test results indicated that both the stress–strain behavior and peak strength of the granular materials were dependent on particle morphology and α_σ. Specifically, the peak strength of the granular materials initially decreased with α_σ, reached its minimum value at approximately α_σ=60°, and then slightly increased. Besides, the increase in particle shape irregularity and surface roughness resulted in enhanced strength. Particle shape tended to have a more substantial impact than surface roughness due to the fact that sphere particles with very high roughness failed to surpass angular particles in terms of strength. Additionally, during the initial phases of shear, variations in α_σ resulted in significant alterations in the stress–dilatancy relationship. Moreover, for nonspherical particles, the stress ratio corresponding to the PTS points exhibited a general decreasing trend with an increase in α_σ.

The strength anisotropy was observed to be more pronounced in granular materials with irregular-shaped particles compared to those with spherical particles. Although granular materials with irregular shapes had higher peak strengths when subjected to a vertical major principal stress axis, their peak strengths exhibited a significantly greater degradation with α_σ in comparison to granular materials with spherical shapes. CT results revealed that particle packings prepared using the dry tamping method tended to orient nearly horizontal. The fabric anisotropy was quantified in this study by the magnitude of the vector (Δ), which described the degree of anisotropy within the fabric tensor. It was discovered that irregular-shaped materials displayed broader preferred particle orientations compared to relatively regular-shaped materials. As sphericity, roundness, and aspect ratio decreased, the initial fabric of the packings exhibited greater anisotropy and Δ generally increases. It was evident that the increased fabric anisotropy induced by irregular particle shapes contributed to the observed increase in strength anisotropy. Notably, a strong relationship was discovered between Δ and the strength anisotropy factor (A_η). With increasing Δ, A_η exhibited a significant increase initially, followed by stabilization. Correlations between parameters Δ and A_η, as well as Δ and various particle morphological factors, have been established. In addition, an anisotropic failure criterion based on the generalization of Lade's (1977) failure criterion was employed to describe the strength failure envelope of granular materials with varying shapes.

Fig. 16. Calibration and verification of isotropic failure criteria: (*a*) $I_1^3/I_3 - 27$ versus A; (*b*) predictions of friction angles; and (*c*) predictions of strength failure envelopes. CDG, completely decomposed granite.

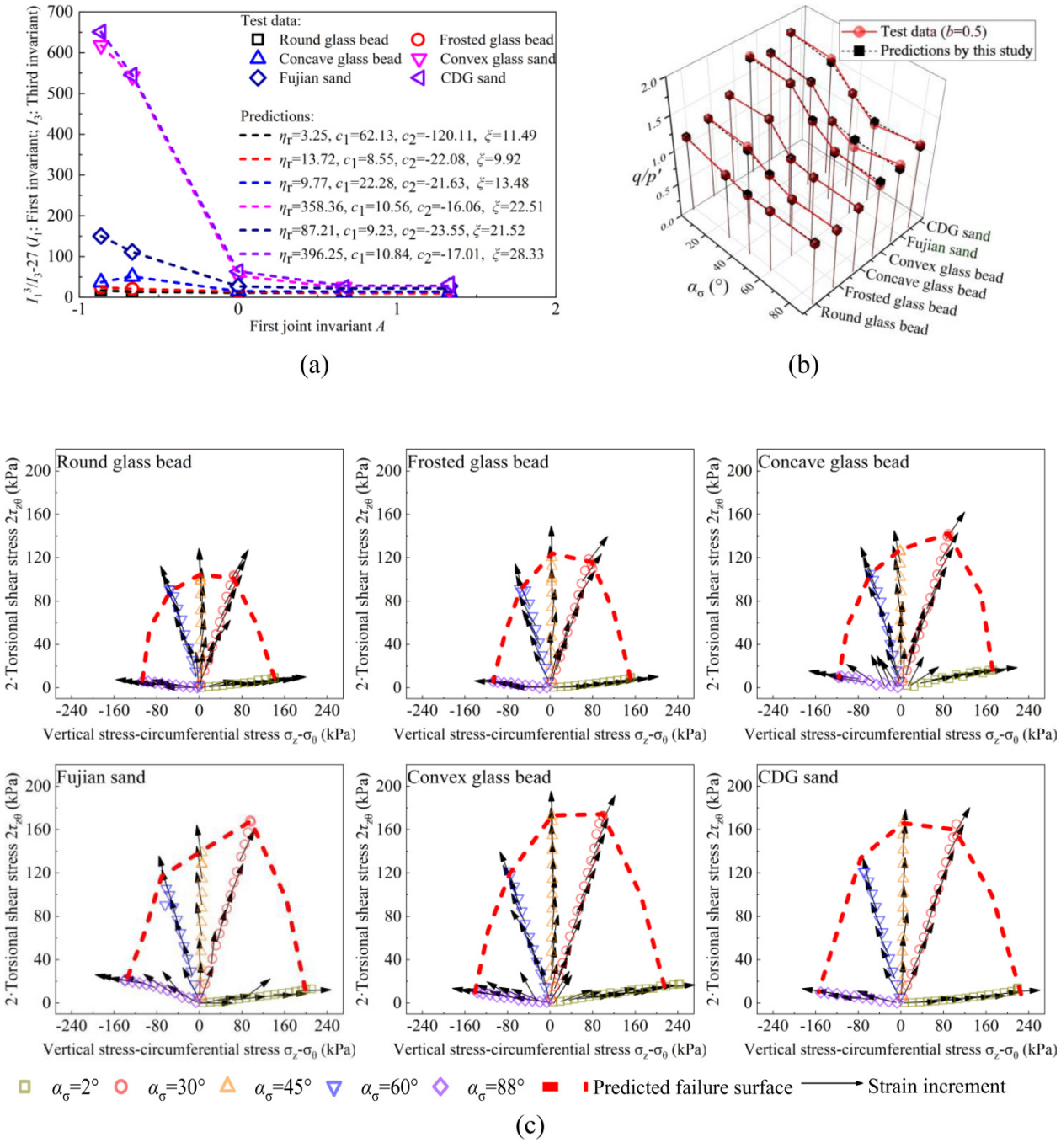

This study focused on investigating the impact of particle shape on the strength and fabric anisotropy of various granular materials prepared using identical methods. Different preparation techniques may result in different preferred orientations of the major axes of granular materials with various particle shapes, thereby causing variations in anisotropic behavior. This aspect will be further explored in future research. Moreover, the developed failure criterion can describe the anisotropic strength of granular materials with different particle morphology, with a particular focus on the innovative integration of shape-induced fabric anisotropy. While the failure criterion can describe the shape of the strength envelope for six different materials in the $(\sigma_z - \sigma_\theta)$–$2\tau_{z\theta}$ plane, its specific relationships require further validation to ensure universal applicability across diverse granular materials. This is because the particle shapes of different materials may have more complex, nonlinear relationships with the fabric parameters that were not captured by the limited data adopted in this study. Therefore, the connection between particle shape indices and fabric parameters for more materials is open to discussion and deserving of deeper investigation in future research.

List of symbols

S	sphericity
AR	aspect ratio
C	convexity
R	Roundness
R_a	average roughness
R_q	root mean square roughness
p'	mean effective stress
q	deviatoric stress
α_σ	angle for the major principal stress direction
b	coefficient of intermediate principal stress
A	first joint invariant
A_η	strength anisotropy factor
φ_x, φ_y, and φ_z	angles between the long axis of the particles and the x, y, and z axes, respectively
φ_H	angles between the long axis of the particles and the bedding plane
Δ	vector magnitude to quantify the degree of anisotropy

Acknowledgements

This research was financially supported by the Research Grants Council (RGC) of Hong Kong Special Administrative Region Government (HKSARG) of China (grant Nos. 15229223, 15227923, 15220221, and 15226822) and the Research Centre for Resources Engineering towards Carbon Neutrality (RCRE) of TheHong Kong Polytechnic University (No. 1-BBEM).

Article information

History dates

Received: 14 December 2023
Accepted: 8 October 2024
Accepted manuscript online: 16 October 2024
Version of record online: 23 January 2025

Data availability

Data available upon request.

Author information

Author ORCIDs

Shao-Heng He https://orcid.org/0000-0001-7883-971X
Zhen-Yu Yin https://orcid.org/0000-0003-4154-7304
Zhi Ding https://orcid.org/0000-0003-3066-7394

Author notes

Zhen-Yu Yin served as Editorial Board Member at the time of manuscript review and acceptance; peer review and editorial decisions regarding this manuscript were handled by another editorial board member.

Author contributions

Formal analysis: ZY, RL
Investigation: SH, RL
Methodology: ZY
Project administration: ZY
Resources: ZD
Supervision: ZY
Validation: ZD
Writing – original draft: SH

Competing interests

The authors declare that they have no competing financial interests or personal relationships that could have appeared to affect the work reported in this paper.

References

Adesina, P., O'Sullivan, C., and Wang, T. 2024. DEM study on the effect of particle shape on the shear behaviour of granular materials. Computational Particle Mechanics, **11**(1): 447–466. doi:10.1007/s40571-023-00632-8.

Altuhafi, F., O'Sullivan, C., and Cavarretta, I. 2013. Analysis of an image-based method to quantify the size and shape of sand particles. Journal of Geotechnical and Geoenvironmental Engineering, **139**(8): 1290–1307. doi:10.1061/(ASCE)GT.1943-5606.0000855.

Altuhafi, F.N., Coop, M.R., and Georgiannou, V.N. 2016. Effect of particle shape on the mechanical behavior of natural sands. Journal of Geotechnical and Geoenvironmental Engineering, **142**(12): 04016071. doi:10.1061/(ASCE)GT.1943-5606.0001569.

Azéma, E., Estrada, N., and Radjaï, F. 2012. Nonlinear effects of particle shape angularity in sheared granular media. Physical Review E, **86**(4): 041301. doi:10.1103/PhysRevE.86.041301.

Azéma, E., Radjai, F., and Dubois, F. 2013. Packings of irregular polyhedral particles: strength, structure, and effects of angularity. Physical Review E, **87**(6): 062203. doi:10.1103/PhysRevE.87.062203.

Banerjee, S.K., Yang, M., and Taiebat, M. 2024. Effect of particle shape on cyclic liquefaction resistance of granular materials. Acta Geotechnica, **19**(7): 4503–4518. doi:10.1007/s11440-023-02169-9.

Burgmann, S., Godehardt, M., Schladitz, K., and Breit, W. 2022. Separation of sand and gravel particles in 3D images using the adaptive h-extrema transform. Powder Technology, **404**: 117468. doi:10.1016/j.powtec.2022.117468.

Cai, Y. 2010. An experimental study of non-coaxial soil behaviour using hollow cylinder testing. University of Nottingham Nottingham.

Cai, Y., Yu, H.-S., Wanatowski, D., and Li, X. 2013. Noncoaxial behavior of sand under various stress paths. Journal of Geotechnical and Geoenvironmental Engineering, **139**(8): 1381–1395. doi:10.1061/(ASCE)GT.1943-5606.0000854.

Cai, Y., Hao, B., Gu, C., Wang, J., and Pan, L. 2018a. Effect of anisotropic consolidation stress paths on the undrained shear behavior of reconstituted Wenzhou clay. Engineering Geology, **242**: 23–33. doi:10.1016/j.enggeo.2018.05.016.

Cai, Y., Song, X., Sun, Q., Dong, Q., and Wang, J. 2018b. Drained responses of granular soil sheared under inclined principal stress axes: impact of sample preparation. Engineering Geology, **241**: 33–40. doi:10.1016/j.enggeo.2018.05.002.

Chen, G., Ma, W., Qin, Y., Zhao, K., and Yang, J. 2021. Liquefaction susceptibility of saturated coral sand subjected to various patterns of principal stress rotation. Journal of Geotechnical and Geoenvironmental Engineering, **147**(9): 04021093. doi:10.1061/(ASCE)GT.1943-5606.0002590.

Curray, J.R. 1956. The analysis of two-dimensional orientation data. The Journal of Geology, **64**(2): 117–131. Available from http://www.jstor.org/stable/30060647 [accessed 25 November 2023]. doi:10.1086/626329.

Dafalias, Y.F., Papadimitriou, A.G., and Li, X.S. 2004. Sand plasticity model accounting for inherent fabric anisotropy. Journal of Engineering Mechanics, **130**(11): 1319–1333. doi:10.1061/(ASCE)0733-9399(2004)130:11(1319).

Gao, Z., and Zhao, J. 2012. Efficient approach to characterize strength anisotropy in soils. Journal of Engineering Mechanics, **138**(12): 1447–1456. doi:10.1061/(ASCE)EM.1943-7889.0000451.

Gapinski, B., Wieczorowski, M., Marciniak-Podsadna, L., Dybala, B., and Ziolkowski, G. 2014. Comparison of different method of measurement geometry using CMM, optical scanner and computed tomography 3D. Procedia Engineering, **69**: 255–262. doi:10.1016/j.proeng.2014.02.230.

Gong, J., Pang, X., Tang, Y., Liu, M., Jiang, J., and Ou, X. 2024. Effects of particle shape, physical properties and particle size distribution on the small-strain stiffness of granular materials: a DEM study. Computers and Geotechnics, **165**: 105903. doi:10.1016/j.compgeo.2023.105903.

Gu, Q., König, D., and Goudarzy, M. 2021. Influence of the sample preparation on the mechanical characteristics of Hostun sand. Geotechnical Engineering Journal of the SEAGS & AGSSEA, **51**(4): 42–50.

He, S.-H., Goudarzy, M., Ding, Z., Sun, Y., Xu, T., and Zhang, Q.-F. 2022. Small-strain shear modulus (Gmax) and microscopic pore structure of calcareous sand with different grain size distributions. Granular Matter, **24**(4): 112. doi:10.1007/s10035-022-01270-2.

He, S.-H., Goudarzy, M., Ding, Z., and Sun, Y. 2023. Strength, deformation, and particle breakage behavior of calcareous sand: role of anisotropic consolidation. Journal of Geotechnical and Geoenvironmental Engineering, **149**(3): 04023002. doi:10.1061/JGGEFK.GTENG-10501.

He, S.-H., Yin, Z.-Y., and Ding, Z. 2024. Cyclic liquefaction of granular materials with varied forms under multidirectional loads. Géotechnique, **0**(0): 1–15. doi:10.1680/jgeot.22.00386.

Huo, Y., Leung, Y., and Kwok, C.Y. 2023. Micro-mechanical perspective on the role of particle shape in shearing of sands. Canadian Geotechnical Journal, **60**(10): 1515–1531. doi:10.1139/cgj-2022-0270.

Ito, K., and Xiong, K. 2000. Gaussian filters for nonlinear filtering problems. IEEE Transactions on Automatic Control, **45**(5): 910–927. doi:10.1109/9.855552.

Kumruzzaman, M., and Yin, J.-H. 2010. Influences of principal stress direction and intermediate principal stress on the stress–strain–strength behaviour of completely decomposed granite. Canadian Geotechnical Journal, **47**(2): 164–179. doi:10.1139/T09-079.

Lade, P.V. 1977. Elasto-plastic stress–strain theory for cohesionless soil with curved yield surfaces. International Journal of Solids and Structures, **13**(11): 1019–1035. doi:10.1016/0020-7683(77)90073-7.

Lade, P.V., Nam, J., and Hong, W.P. 2009. Interpretation of strains in torsion shear tests. Computers and Geotechnics, **36**(1): 211–225. doi:10.1016/j.compgeo.2008.02.001.

Lade, P.V., Rodriguez, N.M., and Dyck, E.J.V. 2014. Effects of principal stress directions on 3D failure conditions in cross-anisotropic sand. Journal of Geotechnical and Geoenvironmental Engineering, **140**(2): 04013001. doi:10.1061/(ASCE)GT.1943-5606.0001005.

Lashkari, A., Falsafizadeh, S.R., Shourijeh, P.T., and Alipour, M.J. 2020. Instability of loose sand in constant volume direct simple shear tests in relation to particle shape. Acta Geotechnica, **15**(9): 2507–2527. doi:10.1007/s11440-019-00909-4.

Li, W., Kwok, C.Y., Sandeep, C.S., and Senetakis, K. 2019. Sand type effect on the behaviour of sand-granulated rubber mixtures: integrated study from micro- to macro-scales. Powder Technology, **342**: 907–916. doi:10.1016/j.powtec.2018.10.025.

Li, Y. 2013. Effects of particle shape and size distribution on the shear strength behavior of composite soils. Bulletin of Engineering Geology and the Environment, **72**(3): 371–381. doi:10.1007/s10064-013-0482-7.

Li, Y., Otsubo, M., Liu, J., and Kuwano, R. 2024. Effect of particle morphology on stress and strain characteristics of granular materials during triaxial compression. Acta Geotechnica, **19**(5): 2753–2773. doi:10.1007/s11440-023-02190-y.

Liu, T., Wang, X., Ally, H., and Wu, T. 2024a. Effect of particle size and two-dimensional shape on internal friction angle of dry sand using image processing. Advanced Powder Technology, **35**(6): 104467. doi:10.1016/j.apt.2024.104467.

Liu, X., Zhang, X., Kong, L., Yin, S., and Xu, Y. 2022. Shear strength anisotropy of natural granite residual soil. Journal of Geotechnical and Geoenvironmental Engineering, **148**(1): 04021168. doi:10.1061/(ASCE)GT.1943-5606.0002709.

Liu, X., Huang, L., Xu, X., Wei, X., and Chen, J. 2023. On unified characterization of wave velocity of sand: a focus on effect of particle shape. Soil Dynamics and Earthquake Engineering, **170**: 107904. doi:10.1016/j.soildyn.2023.107904.

Liu, Y., Liu, X., and Ren, J. 2024b. Effect of particle shape on contact network and shear-induced anisotropy of granular assemblies: a DEM perspective. Journal of Geotechnical and Geoenvironmental Engineering, **150**(3): 04023142. doi:10.1061/JGGEFK.GTENG-11762.

Lorensen, W.E., and Cline, H.E. 1998. Marching cubes: a high resolution 3D surface construction algorithm. *In* Seminal graphics: pioneering efforts that shaped the field. pp. 347–353.

Mandolini, A., Diambra, A., and Ibraim, E. 2019. Strength anisotropy of fibre-reinforced sands under multiaxial loading. Géotechnique, **69**(3): 203–216. doi:10.1680/jgeot.17.P.102.

Miura, K., Miura, S., and Toki, S. 1986a. Deformation behavior of anisotropic dense sand under principal stress axes rotation. Soils and Foundations, **26**(1): 36–52. doi:10.3208/sandf1972.26.36.

Nguyen, H.B.K., Rahman, M.M., and Fourie, A.B. 2020. Effect of particle shape on constitutive relation: DEM study. Journal of Geotechnical and Geoenvironmental Engineering, **146**(7): 04020058. doi:10.1061/(ASCE)GT.1943-5606.0002278.

Oda, M. 1972. Initial fabrics and their relations to mechanical properties of granular material. Soils and Foundations, **12**(1): 17–36. doi:10.3208/sandf1960.12.17.

Oda, M., and Nakayama, H. 1989. Yield function for soil with anisotropic fabric. Journal of Engineering Mechanics, **115**(1): 89–104. doi:10.1061/(ASCE)0733-9399(1989)115:1(89).

Pietruszczak, S., and Mroz, Z. 2000. Formulation of anisotropic failure criteria incorporating a microstructure tensor. Computers and Geotechnics, **26**(2): 105–112. doi:10.1016/S0266-352X(99)00034-8.

Pietruszczak, S., and Mroz, Z. 2001. On failure criteria for anisotropic cohesive-frictional materials. International Journal for Numerical and Analytical Methods in Geomechanics, **25**(5): 509–524. doi:10.1002/nag.141.

Reddy, N.S.C., He, H., and Senetakis, K. 2022. DEM analysis of small and small-to-medium strain shear modulus of sands. Computers and Geotechnics, **141**: 104518. doi:10.1016/j.compgeo.2021.104518.

Rui, S., Guo, Z., Si, T., and Li, Y. 2020. Effect of particle shape on the liquefaction resistance of calcareous sands. Soil Dynamics and Earthquake Engineering, **137**: 106302. doi:10.1016/j.soildyn.2020.106302.

Rui, S., Guo, Z., Si, T., Zhou, W., and Zha, X. 2021. Particle shape influence on the deformation resistance of carbonate sands under drained condition. Soil Dynamics and Earthquake Engineering, **144**: 106688. doi:10.1016/j.soildyn.2021.106688.

Sandeep, C.S., He, H., and Senetakis, K. 2022. Experimental and analytical studies on the influence of weathering degree and ground-environment analog conditions on the tribological behavior of granite. Engineering Geology, **304**: 106644. doi:10.1016/j.enggeo.2022.106644.

Sarkar, D., Goudarzy, M., and König, D. 2019. An interpretation of the influence of particle shape on the mechanical behavior of granular material. Granular Matter, **21**(3): 53. doi:10.1007/s10035-019-0909-3.

Shi, J., Haegeman, W., and Cnudde, V. 2021. Anisotropic small-strain stiffness of calcareous sand affected by sample preparation, particle characteristic and gradation. Géotechnique, **71**(4): 305–319. doi:10.1680/jgeot.18.P.348.

Shibuya, S., Hight, D.W., and Jardine, R.J. 2003. Four-dimensional local boundary surfaces of an isotropically consolidated loose sand. Soils and Foundations, **43**(2): 89–103. doi:10.1016/S0038-0806(20)30804-0.

Uthayakumar, M., and Vaid, Y.P. 1998. Static liquefaction of sands under multiaxial loading. Canadian Geotechnical Journal, **35**(2): 273–283. doi:10.1139/t98-007.

Xiao, Y., Long, L., Matthew Evans, T., Zhou, H., Liu, H., and Stuedlein, A.W. 2019. Effect of particle shape on stress-dilatancy responses of medium-dense sands. Journal of Geotechnical and Geoenvironmental Engineering, **145**(2): 04018105. doi:10.1061/(ASCE)GT.1943-5606.0001994.

Xiao, Y., Fang, Q., Stuedlein, A.W., and Matthew Evans, T. 2023. Effect of particle morphology on strength of glass sands. International Journal of Geomechanics, **23**(8): 04023117. doi:10.1061/IJGNAI.GMENG-8661.

Xiong, H., Guo, L., Cai, Y., and Yang, Z. 2016. Experimental study of drained anisotropy of granular soils involving rotation of principal stress direction. European Journal of Environmental and Civil Engineering, **20**(4): 431–454. doi:10.1080/19648189.2015.1039662.

Yang, J., and Luo, X.D. 2015. Exploring the relationship between critical state and particle shape for granular materials. Journal of the Mechanics and Physics of Solids, **84**: 196–213. doi:10.1016/j.jmps.2015.08.001.

Yang, L.T., Li, X., Yu, H.S., and Wanatowski, D. 2016. A laboratory study of anisotropic geomaterials incorporating recent micromechanical understanding. Acta Geotechnica, **11**(5): 1111–1129. doi:10.1007/s11440-015-0423-7.

Yang, Y., Fei, W., Yu, H.-S., Ooi, J., and Rotter, M. 2015a. Experimental study of anisotropy and non-coaxiality of granular solids. Granular Matter, **17**(2): 189–196. doi:10.1007/s10035-015-0551-7.

Yang, Y., Fei, W., Yu, H.-S., Ooi, J., and Rotter, M. 2015b. Experimental study of anisotropy and non-coaxiality of granular solids. Granular Matter, **17**: 189–196. doi:10.1007/s10035-015-0551-7.

Yang, Z.X., Li, X.S., and Yang, J. 2008. Quantifying and modelling fabric anisotropy of granular soils. Géotechnique, **58**(4): 237–248. doi:10.1680/geot.2008.58.4.237.

Yoshimine, M., Ishihara, K., and Vargas, W. 1998. Effects of principal stress direction and intermediate principal stress on undrained shear behavior of sand. Soils and Foundations, **38**(3): 179–188. doi:10.3208/sandf.38.3_179.

Zamanian, M., Payan, M., Jafarzadeh, F., Ranjbar, N., and Senetakis, K. 2021. Evolution of dynamic properties of cross-anisotropic sand subjected to stress anisotropy. Journal of Geotechnical and Geoenvironmental Engineering, **147**(7): 04021048. doi:10.1061/(ASCE)GT.1943-5606.0002541.

Zdravkovic, L., and Jardine, R.J. 2000. Undrained anisotropy of K0-consolidated silt. Canadian Geotechnical Journal, **37**(1): 178–200. doi:10.1139/t99-094.

Zhao, S., Zhang, N., Zhou, X., and Zhang, L. 2017. Particle shape effects on fabric of granular random packing. Powder Technology, **310**: 175–186. doi:10.1016/j.powtec.2016.12.094.

Zheng, J., and Hryciw, R.D. 2015. Traditional soil particle sphericity, roundness and surface roughness by computational geometry. Géotechnique, **65**(6): 494–506. doi:10.1680/geot.14.P.192.

Zhuang, H., Wang, J., and Gao, Z. 2022. Anisotropic and noncoaxial behavior of soft marine clay under stress path considering the variation of principal stress direction. International Journal of Geomechanics, **22**(6): 04022062. doi:10.1061/(ASCE)GM.1943-5622.0002390.

Appendix A

To determine the orientation of grains, the principal component analysis was utilized. Assuming there are n points on the grain surface, the mean coordinate value of the vertices in the triangular mesh can be expressed as follows:

$$c = \frac{1}{n}\sum_{i=1}^{n} p_i \tag{A1}$$

where c denotes the mean coordinate value of the vertices in the triangular mesh, n is the number of vertices, and p_i refers to the coordinate of ith vertex. Next, we subtract the mean value from the original point cloud to obtain the matrix M:

$$M = [p_1 - c, \ldots, p_n - c] \tag{A2}$$

Subsequently, the covariance matrix of M is determined as follows:

$$C_{\mathrm{M}} = M^{\mathrm{T}}M \tag{A3}$$

Here, M^{T} represents the transposition of matrix M. The eigenvalue equation can be solved as follows:

$$\Lambda V = C_{\mathrm{M}}V \tag{A4}$$

Here, we can obtain a diagonal matrix Λ, comprised of the eigenvalues as its diagonal elements, and the eigenvector matrix V, which contains the eigenvectors as its columns. Given the required eigenvectors and the corresponding eigenvalues, C_{M} can be rewritten as

$$C_{\mathrm{M}} = V\Lambda V^{-1} = \sum_{i=0}^{2} \lambda_i \upsilon_i \upsilon_i^T \tag{A5}$$

$$\Lambda = \mathrm{diag}(\lambda_1, \lambda_2, \lambda_3) \tag{A6}$$

where λ_{i} and υ_i are the ith eigenvalue and eigenvector, respectively. Generally, the eigenvector with the largest eigenvalue is regarded as the major axis or orientation of grains.

Appendix B

For soils with cross anisotropy, the fabric tensor F has been widely adopted as a means of describing the cross anisotropy (Oda and Nakayama 1989):

$$F_{ij} = \begin{bmatrix} F_z & 0 & 0 \\ 0 & F_x & 0 \\ 0 & 0 & F_y \end{bmatrix} = \frac{1}{3+\Delta}\begin{bmatrix} 1-\Delta & 0 & 0 \\ 0 & 1+\Delta & 0 \\ 0 & 0 & 1+\Delta \end{bmatrix} = \frac{1}{3}\begin{bmatrix} 1 & 0 & 0 \\ 0 & 1 & 0 \\ 0 & 0 & 1 \end{bmatrix} + \frac{2\Delta}{9+3\Delta}\begin{bmatrix} -2 & 0 & 0 \\ 0 & 1 & 0 \\ 0 & 0 & 1 \end{bmatrix} \tag{B1}$$

Δ in eq. (B1) was originally used by Oda and Nakayama (1989) to measure the anisotropy distribution of nonspherical particles in granular materials, which is determined in Section 4.2.

The general form of first joint invariant A can be expressed as:

$$A = \frac{s_{ij}d_{ij}}{\sqrt{s_{mn}s_{mn}}\left(\sqrt{d_{mn}d_{mn}}\right)^2} \tag{B2}$$

where s_{ij} ($= \sigma_{ij} - p'\,\delta_{ij}$) and d_{ij} ($= F_{ij} - F_{kk}\delta_{ij}/3$) are the deviatoric portions of the stress tensor σ_{ij} and fabric tensor F_{ij}, respectively. For the representative element in the torsional shear tests, the deviatoric fabric tensor can be expressed as (Gao and Zhao 2012):

$$d_{ij} = \begin{bmatrix} d_z & 0 & 0 \\ 0 & d_\theta & 0 \\ 0 & 0 & d_r \end{bmatrix} = \frac{2\Delta}{9+3\Delta}\begin{bmatrix} -2 & 0 & 0 \\ 0 & 1 & 0 \\ 0 & 0 & 1 \end{bmatrix} \tag{B3}$$

The deviatoric stress components applied on the representative element is (Gao and Zhao 2012):

$$s_{ij} = \begin{bmatrix} s_z & s_{z\theta} & 0 \\ s_{\theta z} & s_\theta & 0 \\ 0 & 0 & s_r \end{bmatrix} = \frac{s_3}{1+b}\begin{bmatrix} 1+b-3\cos^2\alpha_\sigma & -3\sin\alpha\cos\alpha_\sigma & 0 \\ -3\sin\alpha_\sigma\cos\alpha_\sigma & 3\cos^2\alpha_\sigma+b-2 & 0 \\ 0 & 0 & 1-2b \end{bmatrix} \tag{B4}$$

where $s_3(\leq 0)$ = minor deviatoric principal stress. Then, to facilitate the criterion description and parameter calibration, the expression for A derived from eq. (B2) under a typical torsional shear test, i.e., HCA, condition is (Gao and Zhao 2012):

$$A = \frac{-3\cos^2\alpha_\sigma + (b+1)}{2\sqrt{b^2-b+1}} \tag{B5}$$

where α_σ represents the angle of major principal stress direction with respect to the normal axis of bedding plane.

The form of anisotropic interpolation function can be expressed as (Gao and Zhao 2012; Pietruszczak and Mroz 2000, 2001)

(B6) $$g(A, \Delta) = \Delta\left[c_1(1+A) + c_2(1+A)^2 \ldots . c_n(1+A)^n\right]$$

The equations of first, second, third, and fourth order were utilized to determine the most appropriate equation of the lowest order that would yield the best fit with the data. After assessing the fitting results, it was determined that a second-order equation provided a sufficiently good fit:

(B7) $$g(A, \Delta) = \Delta\left[c_1(1+A) + c_2(1+A)^2\right]$$

where c_1 and c_2 are model parameters.